

SN 2018zd: An Unusual Stellar Explosion as Part of the Diverse Type II Supernova Landscape

Jujia Zhang,^{1,2,3,4*} Xiaofeng Wang,^{5,6} József Vinkó^{7,8,9} Qian Zhai,^{1,2,3,4} Tianmeng Zhang,¹⁰ Alexei V. Filippenko,^{12,13} Thomas G. Brink,¹² WeiKang Zheng,¹² Łukasz Wyrzykowski,¹⁴ Przemysław Mikołajczyk,¹⁴ Fang Huang,¹⁵ Liming Rui,⁵ Jun Mo,⁵ Hanna Sai,⁵ Xinhan Zhang,⁵ Huijuan Wang,^{10,11} James M. DeKacy,¹⁶ Eddie Baron,¹⁶ K. Sárneczky,⁷ A. Bódi,^{7,18} G. Csörnyei,^{7,8} O. Hanyecz,⁷ B. Ignácz,⁷ Cs. Kalup,^{7,8,18} L. Kriskovics,^{7,8} R. Könyves-Tóth,^{7,8} A. Ordasi,⁷ A. Pál,^{7,8,17} Á. Sódor,^{7,18} R. Szakáts,⁷ K. Vida,^{7,8,18} G. Zsidi^{7,8,19}

¹Yunnan Observatories (YNAO), Chinese Academy of Sciences (CAS), Kunming, 650216, China

²Chinese Academy of Sciences South America Center for Astronomy, National Astronomical Observatories, CAS, Beijing 100012, China

³Key Laboratory for the Structure and Evolution of Celestial Objects, CAS, Kunming, 650216, China

⁴Center for Astronomical Mega-Science, CAS, 20A Datun Road, Chaoyang District, Beijing, 100012, China

⁵Physics Department and Tsinghua Center for Astrophysics (THCA), Tsinghua University, Beijing, 100084, China

⁶Beijing Planetarium, Beijing Academy of Science and Technology, Beijing, 100044, China

⁷Konkoly Observatory, CSFK, Konkoly-Thege M. ut 15-17, Budapest, 1121, Hungary

⁸ELTE Eötvös Loránd University, Institute of Physics, Pázmány Péter sétány 1/A, Budapest, 1117, Hungary

⁹Department of Optics and Quantum Electronics, University of Szeged, Dóm tér 9, Szeged, 6720, Hungary

¹⁰Key Laboratory of Optical Astronomy, National Astronomical Observatories, Chinese Academy of Sciences, Beijing, 100012, China

¹¹School of Astronomy and Space Science, University of Chinese Academy of Sciences, 101408, Beijing, China

¹²Department of Astronomy, University of California, Berkeley, CA 94720-3411, USA

¹³Miller Senior Fellow, Miller Institute for Basic Research in Science, University of California, Berkeley, CA 94720, USA

¹⁴Astronomical Institute University of Wrocław, M. Kopernika 11, 51-622 Wrocław, Poland

¹⁵Department of Astronomy, Shanghai Jiao Tong University, Shanghai, 200240, China

¹⁶Homer L. Dodge Department of Physics and Astronomy, University of Oklahoma, Norman, OK 73019, USA

¹⁷ELTE Eötvös Loránd University, Department of Astronomy, Pázmány Péter sétány 1/A, Budapest, 1117, Hungary

¹⁸MTA CSFK Lendület Near-Field Cosmology Research Group, Konkoly Observatory, Budapest, 1121, Hungary

¹⁹European Southern Observatory, Karl-Schwarzschild-Strasse 2, 85748 Garching bei München, Germany

Accepted 2020 July 28. Received 2020 April 11; in original form 2020 April 11

ABSTRACT

We present extensive observations of SN 2018zd covering the first ~ 450 d after the explosion. This SN shows a possible shock-breakout signal ~ 3.6 hr after the explosion in the unfiltered light curve, and prominent flash-ionisation spectral features within the first week. The unusual photospheric temperature rise (rapidly from $\sim 12,000$ K to above $18,000$ K) within the earliest few days suggests that the ejecta were continuously heated. Both the significant temperature rise and the flash spectral features can be explained with the interaction of the SN ejecta with the massive stellar wind ($0.18^{+0.05}_{-0.10} M_{\odot}$), which accounts for the luminous peak ($L_{\max} = [1.36 \pm 0.63] \times 10^{43} \text{ erg s}^{-1}$) of SN 2018zd. The luminous peak and low expansion velocity ($v \approx 3300 \text{ km s}^{-1}$) make SN 2018zd to be like a member of the LLEV (luminous SNe II with low expansion velocities) events originated due to circumstellar interaction. The relatively fast post-peak decline allows a classification of SN 2018zd as a transition event morphologically linking SNe IIP and SNe IIL. In the radioactive-decay phase, SN 2018zd experienced a significant flux drop and behaved more like a low-luminosity SN IIP both spectroscopically and photometrically. This contrast indicates that circumstellar interaction plays a vital role in modifying the observed light curves of SNe II. Comparing nebular-phase spectra with model predictions suggests that SN 2018zd arose from a star of $\sim 12 M_{\odot}$. Given the relatively small amount of ^{56}Ni ($0.013 - 0.035 M_{\odot}$), the massive stellar wind, and the faint X-ray radiation, the progenitor of SN 2018zd could be a massive asymptotic giant branch star which collapsed owing to electron capture.

Key words: supernovae: general – supernovae: individual (SN 2018zd).

1 INTRODUCTION

Type II supernovae (SNe II) are hydrogen-rich core-collapse events that are observationally divided into Type IIP (SNe IIP), Type IIL (SNe IIL), Type IIn (SNe IIn), and Type IIb (SNe IIb) (for reviews, see, e.g., Filippenko 1997; Gal-Yam 2017). Among them, SNe IIP belong to the most abundant subclass, which is characterised by a relatively constant optical luminosity plateau lasting for about three months (~ 100 d) after the explosion, followed by a rapid drop to the radioactive tail. The thermalisation of the initial shock wave and the recombination of the ionised hydrogen provide sources to power the plateau light curve (Popov 1993). SNe IIL were named after their linear (in magnitudes) light-curve decay that starts soon after peak brightness. Based on the understanding of SNe IIP, the absence of a plateau in the light curves of SNe IIL might suggest less energy input at a similar phase, while the absence of an abrupt drop in brightness after a few months might indicate a lower-mass H envelope in their progenitors. However, the higher peak luminosity of SNe IIL (~ 1.5 mag brighter than that of SNe IIP, on average; Patat et al. 1993, 1994; Li et al. 2011; Anderson et al. 2014; Faran et al. 2014b; Sanders et al. 2015) disfavors this hypothesis. The continuous range of early-time light-curve slopes found among SNe II (e.g., Anderson et al. 2014; Sanders et al. 2015), and the observed transitional events (e.g., SN 2013ej, Huang et al. 2015; SN 2013by, Valenti et al. 2015) tends to suggest a continuous progenitor population for SNe IIP and SNe IIL.

A fraction of SNe II exhibit signatures of ejecta interaction with circumstellar material (CSM) produced by mass loss in massive stars, especially at their late phases before core collapse. The events that present prominent interaction signatures are classified as SNe IIn (Schlegel 1990). The observed diversity of SNe IIn indicates that the circumstellar environments around their progenitors are complicated. The duration of interaction has large scatter, spanning from a few days (e.g., SN 2013fs, Yaron et al. 2017), a few weeks (e.g., SN 1998S, Fassia et al. 2000; Leonard et al. 2000), a few months (e.g., SN 2010jl, Zhang et al. 2012; Fransson et al. 2014), to even a few years (e.g., SN 2015da, Tartaglia et al. 2020).

The spectra of SNe IIb are similar to those of the SNe IIP and IIL (with strong lines of H) near maximum light, but in the following weeks they usually metamorphose into SNe Ib (Filippenko 1988; Filippenko, Matheson, & Ho 1993). We do not discuss SNe IIb in this paper because they show more similarities to hydrogen-poor events (SNe Ibc, Arcavi et al. 2012; Stritzinger et al. 2018).

The physical origin of SNe IIP and IIL, and their connections with SNe IIn regarding the physical characteristics of their progenitor scenarios and explosion properties, have been long-standing issues. There are pieces of evidence indicating that the diversity between SNe IIP and IIL can be partly explained with short-lived interaction (Valenti et al. 2015; Morozova, Piro, & Valenti 2017). We present optical and ultraviolet (UV) data for the core-collapse SN 2018zd, obtained through an observational campaign that lasted for about 450 d with several telescopes. This SN shows a series of interaction signatures in both spectra and light curves, as well as a large flux drop before entering the radioactive-decay phase.

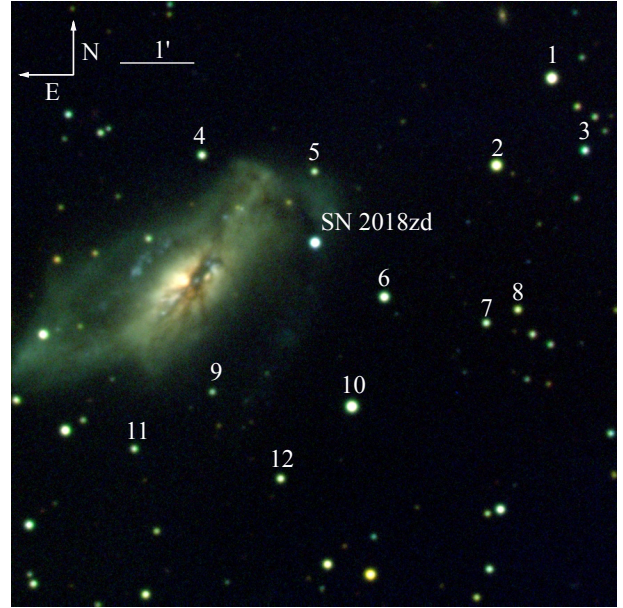


Figure 1. Finder chart of SN 2018zd in NGC 2146. The local reference stars listed in Table A1 are marked with a nearby number. This chart was combined by the *UBV*-band images taken with the 2.4 m LJT and YFOSC on March 7, 2018, with a pixel size of $0.''57$ in the Bin2 readout mode. The average FWHM is $2.''20$ because of the high airmass (~ 1.90) during the observation.

Observations and data reduction are described in Section 2. The UV and optical light curves are presented in Section 3, while the spectral evolution is shown in Section 4. In Section 5, we discuss the bolometric light curve, explosion parameters, progenitor properties, velocity evolution, the position of this SN in the SNe II family, and the possibility of originating from the electron-capture channel. A brief conclusion is given in Section 6.

2 OBSERVATIONS

Koichi Itagaki reported the discovery of the transient AT 2018zd in the nearby SB(s)ab galaxy NGC 2146 on March 02.49, 2018 (UT dates are used throughout this paper). This transient was discovered at 17.8 mag in an unfiltered image obtained with a 0.5 m reflector at the Takamizawa station of Japan¹. Its J2000 coordinates are $\alpha = 06^{\text{h}}18^{\text{m}}03.18^{\text{s}}$ and $\delta = 78^{\circ}22'00''.90$, which is $104.''5$ west and $35.''6$ north of the centre of the host galaxy.

The earliest spectroscopic observations of AT 2018zd were initiated at Li-Jiang Observatory of Yunnan Observatories (YNAO) with the Li-Jiang 2.4 m telescope (hereafter LJT; Fan et al. 2015) equipped with the YFOSC (Yunnan Faint Object Spectrograph and Camera; Wang et al. 2019) only 3 hr after the discovery. However, the noisy spectrum precluded prompt classification of this transient. SN 2018zd was later classified as a young Type IIn SN from a relatively high-quality spectrum obtained at LJT on March 05.74, 2018, which showed narrow emission lines superimposed on a blue continuum (Zhang, Yu, & Wang 2018).

¹ <http://www.k-itagaki.jp>

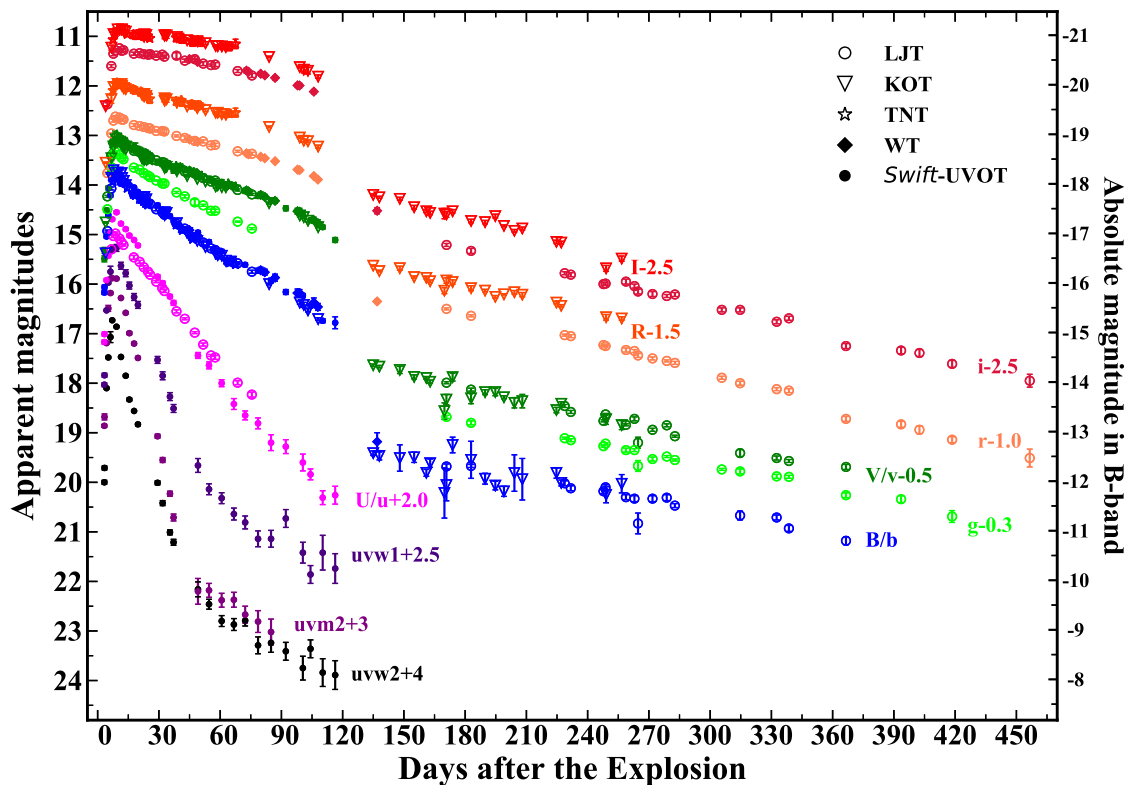


Figure 2. UV-optical light curves of SN 2018zd obtained with the 2.4 m LJT, the 0.8 m KOT, the 0.8 m TNT, the 0.6 m WT, and the *Swift* UVOT. All measurements are shifted vertically for better visibility.

Given the close distance and the young phase when the SN was discovered, we triggered a follow-up observational campaign of SN 2018zd with the LJT of YNAO, the Xing-Long 2.16 m telescope (hereafter XLT), the Tsinghua-NAOC (National Astronomical Observatories of China) 0.8 m telescope (hereafter TNT; Wang et al. 2008; Huang et al. 2012) at Xing-Long Observatory of the NAOC, the 0.6/0.9 m Schmidt telescope (hereafter KOT) of the Konkoly Observatory of the Hungarian Academy of Sciences, and the 0.6 m Cassegrain reflector telescope (hereafter WT) at the Astronomical Observatory of the University of Wrocław, Białkow, Poland (Mikolajczyk & Wyrzykowski 2018). The monitoring spanned from $t \approx 2$ d to $t \approx 456$ d (where t denotes time after the explosion). Late-time spectra were also collected with the 3.5 m Astrophysical Research Consortium (hereafter ARC) telescope of the Apache Point Observatory (APO), and the Keck-I 10 m telescope on Maunakea, Hawai'i. Moreover, the UV-optical photometry spanning from $t \approx 3$ d to $t \approx +116$ d obtained with UVOT on the Neil Gehrels *Swift* Observatory (Gehrels et al. 2004; Roming et al. 2005) is also included here.

2.1 Photometry

SN 2018zd was densely observed by the LJT in the Johnson *UBV* bands and the Sloan *gri* bands, by the TNT and KOT in Johnson *BV* and Cousins *RI*, and by the WT in Johnson *BV* and Sloan *ri*. These images were reduced using

IRAF² standard procedures, including corrections for bias, overscan, flat field, and removal of cosmic rays. The point-spread-function fitting method (Stetson 1987) was used to measure the instrumental magnitudes of the SN. We selected twelve local reference stars in the field of SN 2018zd, as marked in Fig. 1. The instrumental magnitudes of these reference stars are converted to standard *UBVRI* (Vega magnitudes) and *gri* (AB magnitudes) through transformations established by observing a series of Landolt (1992) and Smith et al. (2002) standard stars on some photometric nights, respectively. These magnitudes are applied to calibrate the photometry of SN 2018zd, as presented in Table A2. The photometry of WT is calibrated via the Cambridge Photometric Calibration Server³.

Photometry of SN 2018zd was obtained by the *Swift*/UVOT in three UV filters (*uvw2*, *uvm2*, and *uvw1*) and three broadband optical filters (*u*, *b*, and *v*) and is presented in Table A4. These *Swift* images were reduced using the HEASoft⁴ with the latest *Swift* calibration database⁵.

All of the photometry is presented in Fig. 2, which cov-

² IRAF, the Image Reduction and Analysis Facility, is distributed by the National Optical Astronomy Observatory, which is operated by the Association of Universities for Research in Astronomy (AURA), Inc. under cooperative agreement with the National Science Foundation (NSF).

³ <http://gsaweb.ast.cam.ac.uk/followup>

⁴ HEASoft, the High Energy Astrophysics Software <http://www.swift.ac.uk/analysis/software.php>

⁵ <http://heasarc.gsfc.nasa.gov/docs/heasarc/caldb/swift/>

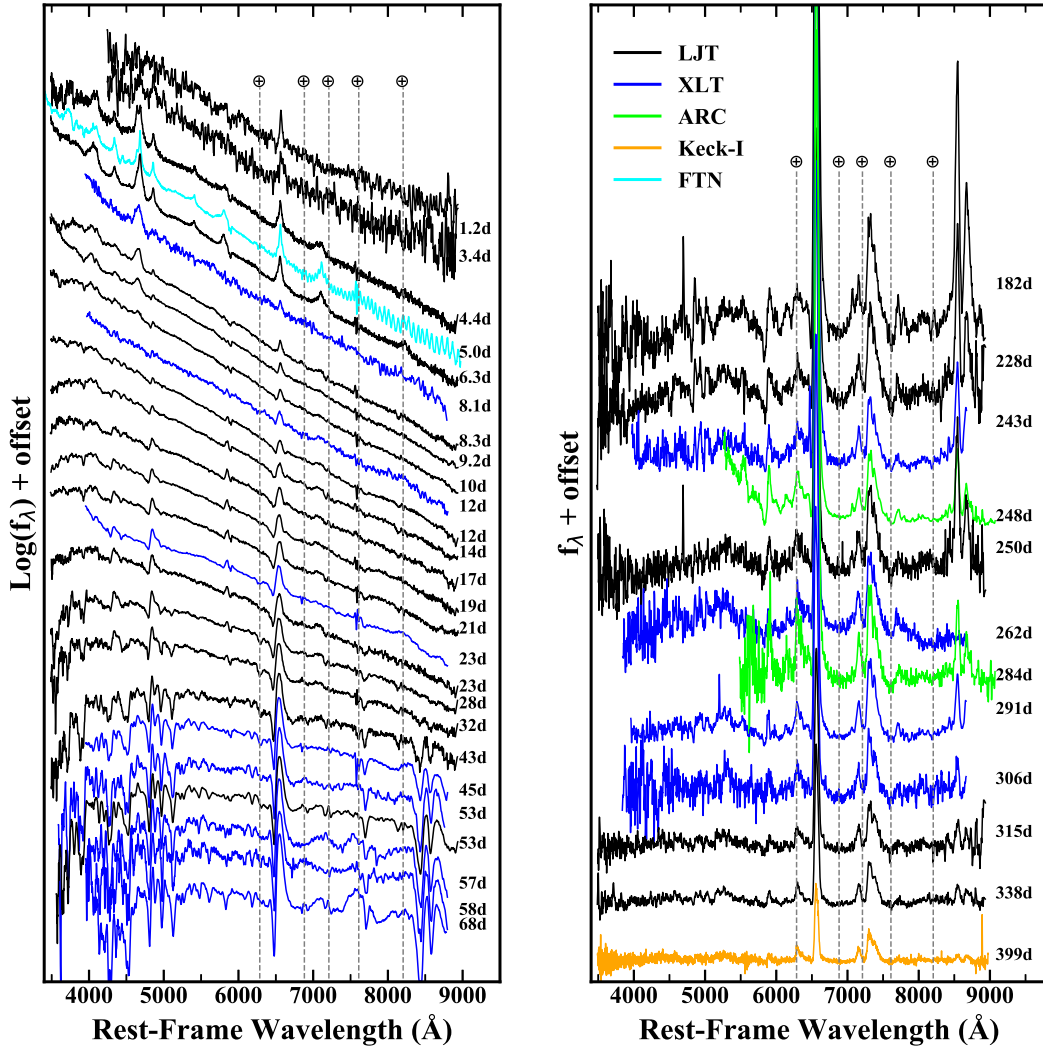


Figure 3. Spectra of SN 2018zd obtained with LJT (black), XLT (blue), ARC (green), Keck-I (orange), and FTN (cyan), shifted vertically for clarity. Regions where telluric absorption was removed (sometimes leaving residuals) are marked with an Earth symbol. Various bin sizes were used for the different spectra, depending on the original signal-to-noise ratio. *Left*: early-phase and photospheric-phase spectra. *Right*: nebular-phase spectra.

ers the first ~ 450 d since discovery. Note that the instrumental response curves of the UVOT optical filters do not follow exactly those of the Johnson *UBV* system, especially in *Swift* *u* where the UVOT coverage is wider than Johnson *U*. Thus, we treat the *u* and *U* bands individually in the following calculation and analysis.

2.2 Spectroscopy

Fig. 3 shows the spectral sequence of SN 2018zd spanning from $t \approx +2$ d to $t \approx +400$ d. The journal of observations is given in Table A5, including twenty-two spectra from LJT (with the YFOSC), twelve from XLT (with the Beijing Faint Object Spectrograph and Camera, BFOSC), two from ARC (with the Dual Imaging Spectrograph, DIS), and one from Keck-I (with the Low-Resolution Imaging Spectrometer, LRIS; Oke et al. 1995). All of these spectra are calibrated in both wavelength and flux, and they are corrected for telluric absorption and redshift. Spectra were ob-

tained with a slit oriented along the parallactic angle to minimise the effects of atmospheric dispersion (Filippenko 1982); moreover, the continuum shape was further corrected with multiband photometry. One spectrum (presented at the transient name system, TNS⁶), obtained using the FLOYDS spectrograph on the Las Cumbres Observatory 2 m Faulkes Telescope North (FTN) on Haleakala, Hawai‘i, is also plotted in this figure to help elucidate the rapid evolution at very early times.

2.3 Distance and extinction

The distance D of SN 2018zd adopted in the following calculation is 18.4 ± 4.5 Mpc, derived from the averaged measurements of the host galaxy (NGC 2146) listed in the NASA/IPAC Extragalactic Database (NED⁷). For exam-

⁶ <https://wis-tns.weizmann.ac.il/object/2018zd>

⁷ <http://ned.ipac.caltech.edu>

Table 1. Photometric Results for SN 2018zd^a

Band	λ_{eff}	FWHM (Å)	t_{rise} (d)	m_{max}^b (mag)	M_{max} (mag)	M_{end} (mag)	M_{tail} (mag)	Δm_{50} (mag)	γ (mag [100 d] ⁻¹)
<i>uvw2</i>	1928	657	6.94(0.05)	12.71(0.03)	-19.97(0.61)	5.94(0.05)	...
<i>uvm2</i>	2246	498	7.27(0.06)	12.83(0.05)	-20.06(0.67)	6.46(0.05)	...
<i>uvw1</i>	2600	693	7.35(0.05)	12.81(0.03)	-19.61(0.54)	4.93(0.04)	...
<i>u</i>	3465	785	8.27(0.05)	12.58(0.02)	-19.54(0.45)	3.30(0.03)	...
<i>U</i>	3652	485	8.46(0.05)	12.97(0.02)	-19.14(0.44)	2.59(0.03)	...
<i>B</i>	4312	831	9.13(0.05)	13.79(0.01)	-18.19(0.41)	-15.93(0.43)	-12.48(0.43)	1.53(0.03)	0.74(0.06)
<i>g</i>	4754	1280	8.77(0.05)	13.62(0.01)	-18.29(0.39)	...	-13.02(0.45)	1.24(0.03)	0.75(0.07)
<i>V</i>	5341	827	8.98(0.05)	13.55(0.01)	-18.26(0.36)	-16.82(0.38)	-13.43(0.38)	0.93(0.03)	0.90(0.07)
<i>r</i>	6196	1150	9.21(0.05)	13.59(0.01)	-18.15(0.34)	-17.14(0.36)	-14.49(0.38)	0.63(0.03)	1.09(0.06)
<i>R</i>	6315	1742	9.28(0.07)	13.45(0.01)	-18.28(0.33)	-17.31(0.36)	-14.37(0.36)	0.60(0.02)	0.80(0.06)
<i>i</i>	7690	1230	9.67(0.05)	13.74(0.01)	-17.88(0.30)	-17.22(0.32)	-14.06(0.35)	0.37(0.02)	0.96(0.06)
<i>I</i>	8752	1970	10.18(0.08)	13.36(0.01)	-18.19(0.28)	-17.50(0.31)	-14.66(0.33)	0.35(0.02)	1.12(0.09)

^aThe *uvw2*, *uvm2*, *uvw1*, and *u* bands of *Swift*/UOVT, and the Johnson *UBVRI* bands, are in the Vega magnitude system. SDSS *gri* bands are in the AB magnitude system. The numbers given in brackets are the 1σ uncertainties. ^bDerived by fitting a cubic polynomial to the points around maximum brightness.

ple, the average estimation from the Tully-Fisher relation is $D = 19.2 \pm 8.8$ Mpc (Bottinelli et al. 1984; Giraud 1985; Tully & Fisher 1988; Schoniger & Sofue 1994; Tutui & Sofue 1997), the measurement via the observed angular radius of typical globular clusters in NGC 2146 (comparing with the physical radii of Milky Way globulars) is 18.0 ± 1.8 Mpc (Adamo et al. 2012), and the result from the radial velocity of NGC 2146 ($v = 1219 \pm 16$ km s⁻¹, after correcting for Local Group infall into the Virgo Cluster, the Great Attractor, and the Shapley Supercluster Mould et al. 2000) is 17.98 ± 1.26 Mpc with $H_0 = 67.8$ km s⁻¹ Mpc⁻¹ (Planck 2014).

In our analysis, we use the interstellar Na I D absorption to estimate the reddening toward SN 2018zd. Two Na I D absorption systems are detected in the spectra of SN 2018zd, with similar equivalent width (EW), $\sim 1.3 \pm 0.1$ Å (see Fig. 8), suggesting significant extinction due to the host galaxy and the Milky Way. The minimum reddening value derived from the existing empirical correlations between reddening and EW of Na I D, $E(B - V) = 0.16 \text{EW} - 0.01$ mag (Turatto et al. 2003), is $E(B - V)_{\text{host}} = E(B - V)_{\text{MW}} = 0.198$ mag. However, the Galactic reddening derived by Schlafly & Finkbeiner (2011) is only $E(B - V)_{\text{MW}} = 0.085$ mag. Considering the large scatter of the reddening measurement via Na I D absorption (e.g., Poznanski et al. 2011), we assume $E(B - V)_{\text{host}} = E(B - V)_{\text{MW}}$ because of the similar EW of Na I D from the host galaxy and the Milky Way. Thus, a total reddening of $E(B - V) = 0.17 \pm 0.05$ mag with the extinction law $R_V = 3.1$ is adopted in this paper. This matches the estimate via the $V - I$ colour in Section 3.4. We caution, however, that the luminosity of SN 2018zd may be underestimated because of the conservative host-galaxy reddening adopted in our analysis.

3 ANALYSIS OF THE PHOTOMETRY

3.1 Explosion date and a shock-breakout signal

To better estimate the explosion date of SN 2018zd, we also collect the clear-band data obtained by amateur astronomers in the early phase of detections⁸, as listed in Table A6. The

clear-band photometry roughly matches that of the *r* band of LJT, as shown in Fig. 4.

A simple expanding fireball model, $F(t) = F_1 \times (t - t_0)^2$, is applied to fit observations at $t \lesssim 8$ d except for the earliest detection. The explosion date derived by the expanding fireball model is $\text{MJD} = 58178.39^{+0.15}_{-0.50}$, which implies that SN 2018zd was first detected (by Itagaki; see below) only 3.6 hr after the explosion. It is reasonable that SN 2018zd was very young at the first detection because its brightness increased by ~ 5 mag when approaching the peak.

Note that Itagaki had a prediscovery detection (obtained with a 0.35 m telescope at Okayama Observatory) at the site of SN 2018zd roughly one day before his official discovery image, with an unfiltered magnitude of 18.0. About 13 hr after this earliest detection, however, Patrick Wiggins⁹ reported a nondetection of SN 2018zd in an unfiltered image with an upper limit of 18.5 mag. Such an intraday dip is very likely related to the shock-breakout phenomenon (as seen in KSN 2011d; Garnavich et al. 2016).

3.2 Photometric results

Table 1 lists estimates of the explosion time to peak brightness (t_{rise}), the apparent (m_{max}) and absolute (M_{max}) magnitude at maximum brightness, the absolute magnitude at the end of the plateau phase (M_{end} , at $t = 125$ d, in the case of SN 2018zd) and at the beginning of the radiative tail (M_{tail} , at $t = 155$ d), the decline rate from peak to 50 d later (Δm_{50}), and the decline rate per 100 d (γ) during the radioactive tail (at $t > 150$ d, when the light curve is powered by radioactive decay and is governed by γ -ray trapping) of SN 2018zd in all bands presented in Fig. 2.

Compared with the sample from Pritchard et al. (2014), the absolute peak magnitudes of SN 2018zd are located at the luminous end of SNe IIP and SNe IIL, and the faint end of SNe IIn. The UV peak of SN 2018zd ($M_{\text{UV}} \approx -20$ mag) is brighter than that of SNe IIP ($M_{\text{UV}} \approx -18$ mag), and is close to the average brightness of SNe IIn ($M_{\text{UV}} \approx -20$ mag). The

⁹ <https://wis-tns.weizmann.ac.il/object/2018zd#comment->

⁸ “Bright Supernovae,” www.rochesterastronomy.org/sn2018/sn2018zd.html paper-1927

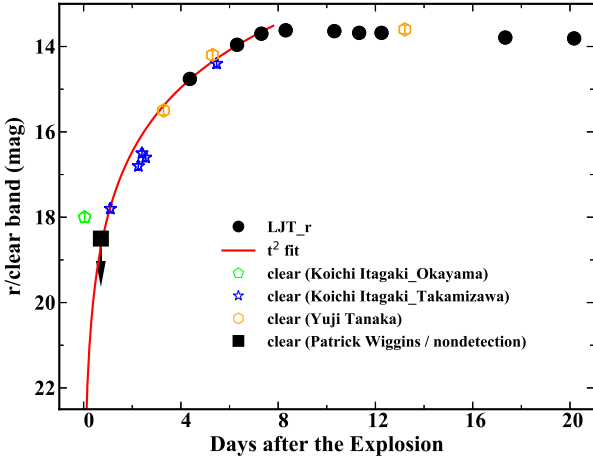


Figure 4. Expanding fireball fit of the early detections of SN 2018zd in the clear band and the r band, where the first detection by Itagaki cannot be fitted.

optical brightness of SN 2018zd (e.g., $M_{\text{Op}} \approx -18$ mag, in the B and V bands) lies between the bright end of SNe IIP ($-18 < M_{\text{Op}} < -15$ mag) and the faint end of SNe IIn ($-20 < M_{\text{Op}} < -18$ mag; Pritchard et al. 2014). Richardson et al. (2002) found that the average B -band peak absolute magnitude is $M_B = -17.0 \pm 1.1$ mag for 29 SNe IIP and $M_B = -18.0 \pm 0.9$ mag for 19 SNe IIL. This indicates that SN 2018zd is brighter than most SNe IIP and comparable to SNe IIL in the optical. Furthermore, considering SNe IIP and IIL as a continuous family, SN 2018zd is at the bright end of the distribution ($-13.77 < M_V < -18.29$ mag; Anderson et al. 2014).

As shown in Fig. 2, the light curve of SN 2018zd had a fast decline from the peak to the plateau phase. Faran et al. (2014b) suggested that SNe II with $\Delta m_{50} > 0.5$ mag in the V band can be classified as SNe IIL. Based on such a criterion, SN 2018zd could be placed into the SN IIL group because of a relatively quick decline (i.e., $\Delta m_{50}^V = 0.93 \pm 0.03$ mag). However, a further significant flux drop can be found at $t \approx 115$ d in the optical light curves, with a decline of ~ 3 mag when entering the radioactive-decay tail. Such a significant flux drop has been regarded as a typical feature of SNe IIP when hydrogen recombination process ends in the envelope.

Nevertheless, Anderson et al. (2014) and Valenti et al. (2015) proposed that if all SNe IIL were monitored sufficiently long, they would exhibit a significant drop in their late-time light curves. SN 2018zd is an excellent example supporting the above argument because of the SN IIL-like initial decline rate and the SN IIP-like drop from the end of plateau to the radioactive tail.

We notice that the UV light curves of SN 2018zd showed an unusually slow increase to peak compared to the optical, reaching maximum brightness ~ 1 week after explosion. However, SNe II usually reach their UV maximum much earlier (at $t \approx 1\text{--}3$ d) than in the optical (~ 5 d in U and ~ 10 d in I). For example, Pritchard et al. (2014) noted that most of their sample were observed before the V -band maximum, but only a few before UV maximum even though some were monitored at quite young phases.

3.3 Morphology of the light curves

The multiband light curves of SN 2018zd are shown in Fig. 5, together with those of some well-observed SNe II. The morphology comparison confirms the results derived in Section 3.2:

- (1) The UV emission of SN 2018zd rises slowly; it reaches the $uvw2$ -band peak $\sim 3\text{--}6$ d later than the other comparison SNe. The rise time of these SNe in the UV band is uncertain because their peaks occur near the time of the first detection. Thus, these events may have reached their maximum brightness a few days earlier than shown in this figure.
- (2) The peak brightness of SN 2018zd is close to that of SNe IIP at the bright end, and it is close to that of SNe IIL and SNe IIn. Among the comparison SNe II, only SN IIn 1998S shows a more luminous peak than SN 2018zd.
- (3) SN 2018zd has an intermediate decline rate during the plateau phase, faster than that of regular SNe IIP (e.g., SN 1999em, SN 2004et, and SN 2017eaw), but slower than that of fast-declining SNe II (e.g., SN 2013ej and SN 2013by).
- (4) SN 2018zd exhibits the most significant drop from the peak to the end of the plateau phase, even greater than that of SN 2013ej and SN 2013by.

3.4 Colour curves

SN 2018zd shows bluer $uvw2-u$ and $B-V$ colours at $t \lesssim 50$ d than normal SNe IIP, as presented in Fig. 6, which might result from the contribution of CSM interaction. Based on a similar argument, it is not surprising that the colour of SN 1998S is bluer than that of SN 2018zd because the former might have stronger interaction.

Different comparison samples of SNe II generally exhibit similar colour evolution but with some notable differences. The most obvious is that SN 2018zd shows a very clear reversal (“U-turn”) in the $uvw2-u$ colour curve at early times. A similar but weaker feature is present in the $B-V$ and $V-I$ colour curves. This U-turn behaviour indicates that the temperature increase of SN 2018zd is consistent with the temperature evolution derived in the following section. Besides, the decreased extinction due to dust destruction at the early phase of the explosion could also explain this U-turn behavior. However, no evidence of dust destruction (e.g., the variation of Na I D absorption from the host galaxy) is found in our low-resolution spectra.

The $uvw2-u$ colour U-turn is not typical of the SN II family even among those with very early-time observations, such as SN 2017eaw and SN 2016X. It is suspected that SN 2013ej, SN 2013by, and SN 2016bkv might also have similar $uvw2-u$ colour evolution, as they show the U-turn feature in the $B-V$ colour curve; however, their UV data are either absent or too poorly sampled for a detailed comparison.

The $uvw2-u$ colour of SN 2018zd becomes bluer again at $t > 40$ d, a reverse “U-turn” shape that is due to the increased H Balmer absorption within the u band and the decreased metal line-blanking in the $uvw2$ band (e.g., see the UV-optical spectral evolution in Figure 2 of Dessart et al. 2013). The similar reverse “U-turn” seen in the $B-V$ and $V-I$ colours at $t \gtrsim 150$ d is related to the evolution of emission lines in the nebular phase. These reverse “U-turn” shapes seen in the colour curves do not imply that the temperature is rising.

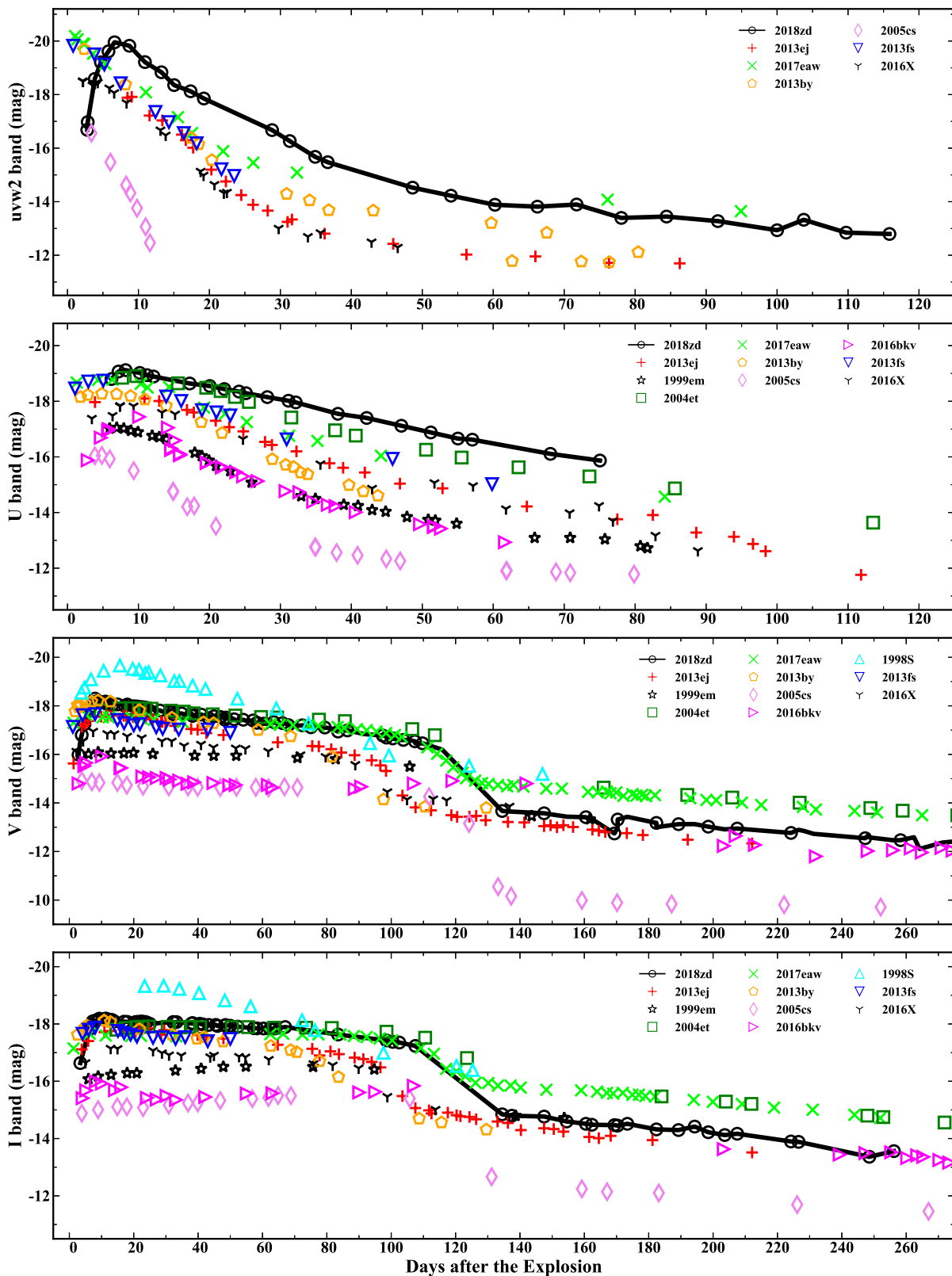


Figure 5. Light-curve comparisons (in absolute magnitude) between SN 2018zd with some well-studied SNe II, including the standard SNe IIP 1999em (Hamuy et al. 2001; Leonard et al. 2002; Elmhamdi et al. 2003) and 2004et (Sahu et al. 2006; Misra et al. 2007), the normal SN IIP 2017eaw (Rui et al. 2019; Szalai et al. 2019, and unpublished data collected with LJT and TNT), the fast-declining SNe II 2013ej (Huang et al. 2015; Dhungana et al. 2016; Yuan et al. 2016) and 2013by (Valenti et al. 2015), the low-velocity and low-luminosity SN IIP 2005cs (Pastorello et al. 2006, 2009), and SNe II showing interaction signatures in their spectra such as SNe 2013fs (Yaron et al. 2017; Bullivant et al. 2018), 2016bkv (Hosseinzadeh et al. 2018; Nakaoka et al. 2018), and 1998S (Leonard et al. 2000; Fassia et al. 2000; Poon et al. 2011).

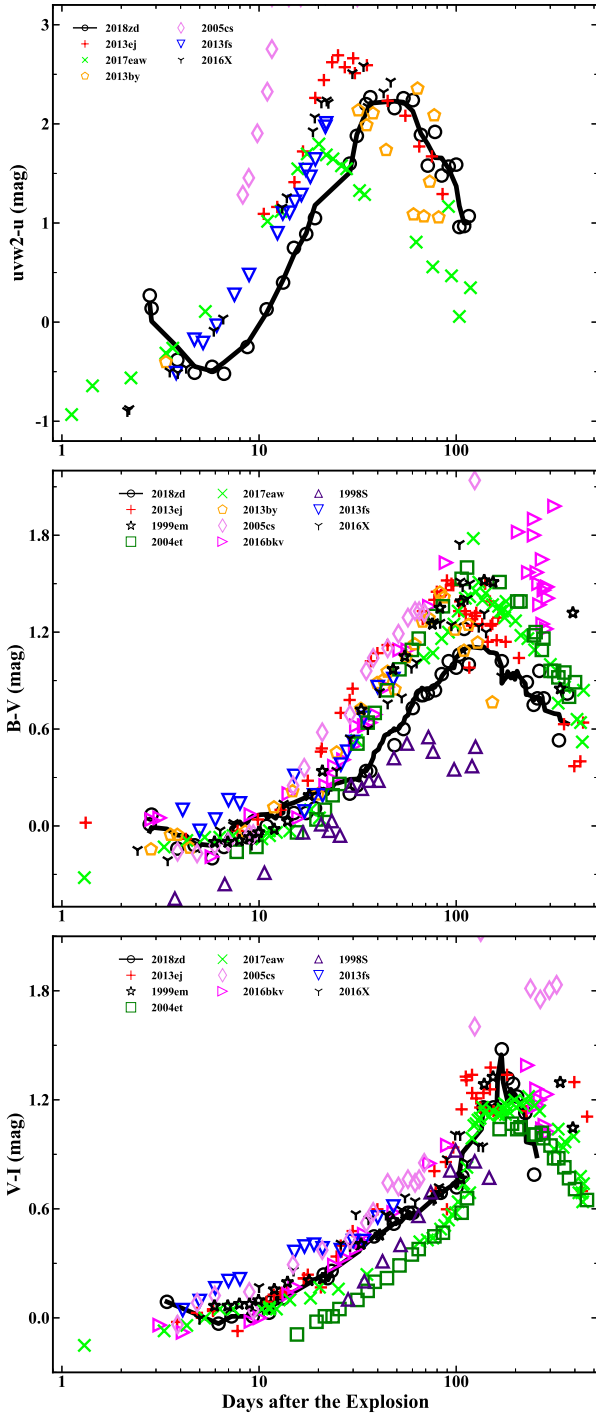


Figure 6. The $uvw2-u$, $B-V$, and $V-I$ colours of SN 2018zd compared with those of the sample presented in Fig. 5. All of these colour curves have been corrected for host-galaxy and Milky-Way extinction.

The intrinsic colour of SNe II could be another way to estimate extinction. For example, Hamuy (2003) suggested using the $V-I$ colour as a better reddening indicator than the $B-V$ colour because it is expected to be less sensitive to metallicity effects. The $V-I$ colour of SN 2018zd roughly follows that of SN 1999em, SN 2013ej, SN 2016X, and SN 2017eaw at $10 < t < 100$ d. This suggests a smaller effect

of interaction in the $V-I$ colour of SN 2018zd than in the bluer colour. Thus, we could estimate the extinction via an empirical relation, such as $A_V(V-I) = \beta_V[(V-I) - 0.656]$ (Olivares et al. 2010), where the $V-I$ colour corresponds to the colour of a given SN 30 d before the end of the plateau, and $\beta_V = A_V/E(V-I)$ is related to R_V (e.g., $\beta_V = 2.518$ for $R_V = 3.1$). Based on the $V-I$ colour of SN 2018zd measured at the appropriate phase ($t \approx 65$ d), the total extinction is estimated to be $A_V^{\text{total}} = 0.52 \pm 0.10$ mag, and $E(B-V)_{\text{total}} = 0.168 \pm 0.033$ for $R_V = 3.1$. These values are consistent with the reddening adopted in this paper.

3.5 Spectral energy distribution

The left panel of Fig. 7 displays the spectral energy distribution (SED) of SN 2018zd at some selected epochs. At $t \lesssim 116$ d, when *Swift*-UVOT observations are available, we construct the SED from the observed fluxes in the UV through optical passbands (covering the wavelength from ~ 1600 to ~ 9700 Å) obtained at the same phase. The missing data are obtained through interpolation of the adjacent data. The SEDs at $t > 155$ d are constructed only from the *BVRI* or the *BgVri* photometry.

The SED peaks toward shorter wavelengths in the first few days and then toward longer wavelengths, which conforms to an initial heating followed by cooling processes as indicated in the temperature curve presented in the right panel of Fig. 7. The temperature of SN 2018zd is derived via blackbody fitting of the SED; it increases from $\sim 12,000$ K to $\sim 18,000$ K in the first week after the explosion. This behaviour might be related to CSM interaction at early times, as is also indicated by the early spectra (see Fig. 8). At these phases, the forward shock accelerates and heats the shocked wind/CSM and the reverse shock reheats the outer layers of the ejecta (Branch & Wheeler 2017).

For SNe II, it is not common to see the temperature increase at early times. Hosseinzadeh et al. (2018) reported the unexpected temperature rise of SN 2016bkv during a similar period. However, their conclusion is uncertain, owing to a lack of near-UV photometry. Thus, SN 2018zd could be the first SN II for which there is conclusive evidence of a rising temperature at early phases.

The right-hand panel of Fig. 7 also displays the photospheric radius (R) of SN 2018zd calculated from the relation $L = 4\pi\sigma R^2 T^4$, where the luminosity L is derived by integrating the SED from 1600 Å to $27,000$ Å; flux outside the wavelength range of photometric coverage is extrapolated based on a blackbody spectrum.

The photospheric radius of SN 2018zd is $R = (3.57 \pm 0.50) \times 10^3 R_\odot$ at $t \approx 2.9$ d, increasing slowly during the temperature rising phase. After ~ 40 d of faster expansion, SN 2018zd reached maximum photospheric radius ($R \approx 2.5 \times 10^4 R_\odot$) at $t \approx 45$ d and remained almost unchanged during the next two months; thus, recombination provided the dominant source of energy at this phase. The recombination temperature is ~ 6000 K, so the ejecta consist of a mixture of hydrogen and helium (Grassberg & Nadyozhin 1976). The photospheric radius decreases when recombination ends and the SN envelope becomes transparent.

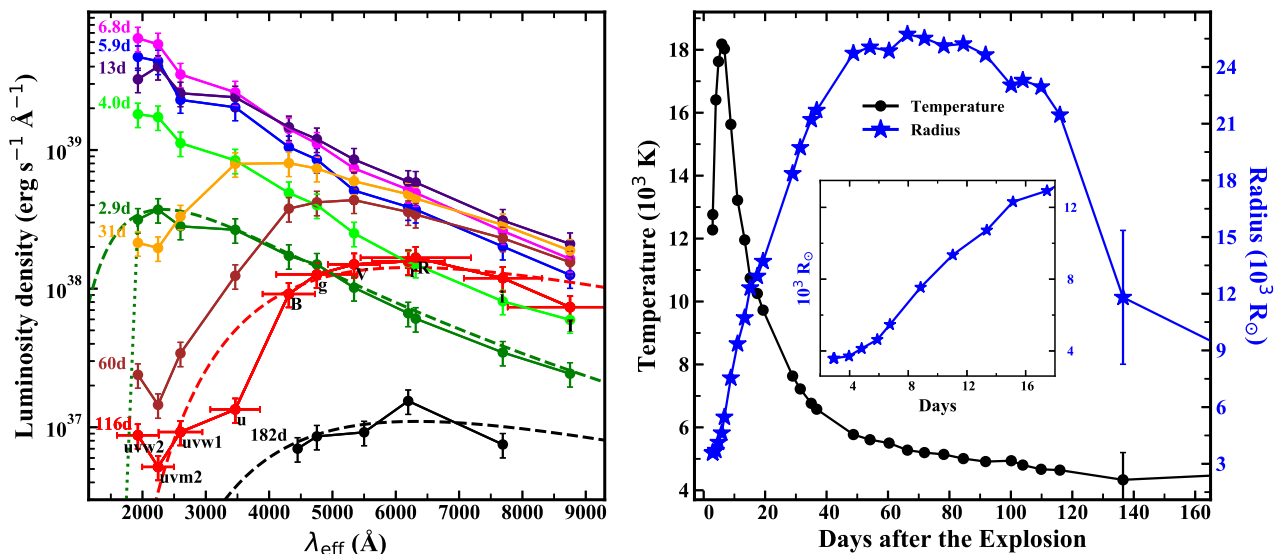


Figure 7. *Left:* SED of SN 2018zd at selected phases. The dashed lines are examples of blackbody fits to the observations at $t = 2.9$ d and 182 d. The dotted-line is the flux extrapolation of the flux at the wavelength shorter than 1928\AA , the flux at the wavelength shorter than 1216\AA goes to zero due to the absorption of H-rich atmosphere. The uncertainty of each SED is about 20%, including errors in photometry, extinction, and distance. *Right:* Temporal evolution of the temperature and the photospheric radius of SN 2018zd. The inset shows a close-up view of the radius at $t < 18$ d. The typical uncertainty of the temperature is about 20%, including errors in photometry, extinction, and blackbody fitting. The typical uncertainty of the radius is about 30%, including errors in temperature and distance, see the sample errors at $t \approx 137$ d.

4 SPECTROSCOPIC ANALYSIS

Fig. 8 displays the spectral comparison of SN 2018zd with a selected sample and model spectra obtained at different phases, including the flash-ionisation, photospheric, and nebular phases.

4.1 Flash-ionisation phase

Panel (a) of Fig. 8 displays early-time spectra of SN 2018zd at $t \lesssim 10$ d, together with that of SN 1998S, SN 2013fs, and the r1w5h model spectra given by Dessart, Hillier, & Audit (2017) at similar phases. The spectra of SN 2018zd are dominated by flashed-ionised features (Gal-Yam et al. 2014) such as the narrow emission lines of hydrogen, N v $\lambda\lambda 4334, 4641$, He II $\lambda 4686$, He II $\lambda 4860$, C IV $\lambda\lambda 5801, 5812$, and C IV $\lambda 7110$. These features are generated by the surrounding wind material which was ionised by X-rays from the shocked ejecta (Branch & Wheeler 2017). The first two low-quality spectra of SN 2018zd in Fig. 3 show possible H α emission, suggesting that the interaction starts ~ 1.2 d after explosion.

The flash features in SN 2018zd appear to evolve more slowly than in SN 2013fs. A noticeable change from $t \approx 4.4$ d to $t \approx 6.3$ d is the weakening of N v $\lambda\lambda 4634, 4641$, which suggests a decreasing ionisation. However, this seems to conflict with the increasing surface temperature inferred at this phase (see Section 3.5); perhaps the temperature derived from the SED may not fully reflect radiation in the ionisation region.

The spectra of SN 1998S at $t \approx 2.3$ d and 3.3 d are similar to that of SN 2018zd at $t \approx 4.4$ d. The similarity of the two spectra of SN 1998S (separated by 1 d) might suggest slower spectral evolution than that of SN 2018zd. In contrast, SN 2013fs went through very rapid changes during the first few

days after the explosion. The narrow emissions seen in SN 2013fs showed pronounced variations on a timescale of hours and almost vanished ~ 2 d after the explosion.

Dessart, Hillier, & Audit (2017) applied radiation hydrodynamics and nonlocal-thermodynamic-equilibrium (NLTE) radiative transfer to produce observational features of SNe II with short-lived flash spectra considering different physical states of the progenitor before the explosion. The ionisation features produced in the r1w5h (where r1 means the progenitor star radius with $R_{\star} = 501 R_{\odot}$, w5 means a wind mass-loss rate of $\dot{M} = 5 \times 10^{-3} M_{\odot} \text{yr}^{-1}$, and h means the atmospheric density scale height of $H_{\rho} = 0.1 R_{\star}$) model is the closest to that seen in SN 2018zd among their models.

One can see that the r1w5h model can reproduce the dominant spectral features observed in SN 2018zd, but the model evolves too fast. For example, the model spectrum at $t \approx 0.8$ d shows a similar continuum and spectral features (e.g., N v and He II lines) as the $t \approx 4.4$ d spectrum of SN 2018zd. The Balmer lines in the model spectrum are weaker than those of SN 2018zd. The model spectrum at $t = 1.0$ d exhibits line features similar to those in the $t \approx 8.3$ d spectrum of SN 2018zd. The continuum of the featureless model spectrum at $t = 2.0$ d has a slope similar to that of SN 2018zd at $t \approx 8.3$ d.

The slower spectral evolution and the longer-lived flash features of SN 2018zd in comparison with SN 2013fs and the r1w5h model are consistent with the slower light-curve rise seen in SN 2018zd. This difference might suggest a more massive and extended stellar wind surrounding SN 2018zd. On the other hand, the spectral evolution of SN 2018zd during the flash phase seems to be faster than that of SN 1998S. Therefore, we propose that SN 2018zd might have an environment (e.g., the mass of wind/CSM) lying between that

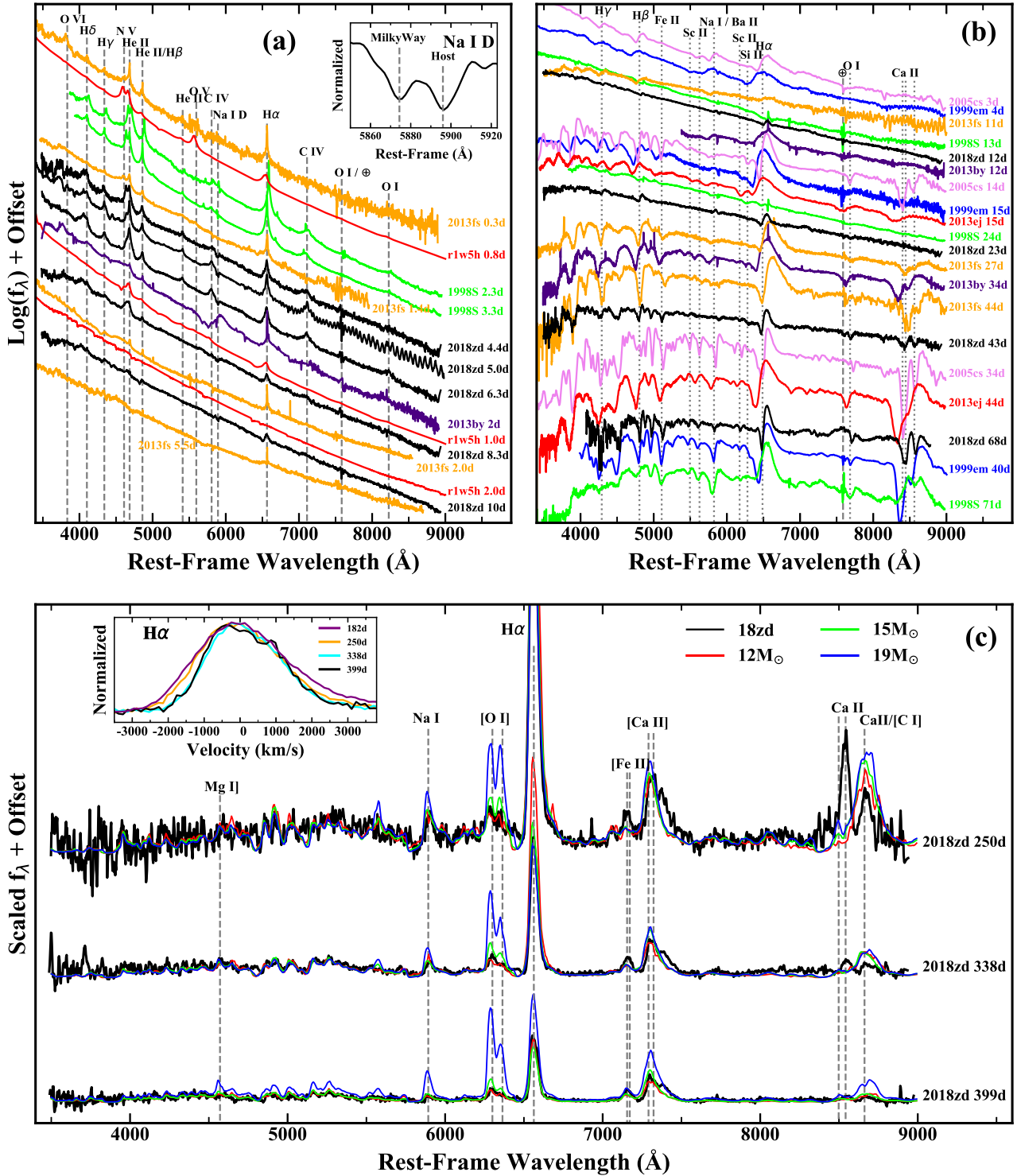


Figure 8. Spectral comparison at three phases. (a) Flash-ionisation-phase spectra of SN 2018zd compared with spectra of SN 1998S (Leonard et al. 2000; Fassia et al. 2001; Shivvers et al. 2015), SN 2013by (Valenti et al. 2015), SN 2013fs (Yaron et al. 2017), and model spectra r1w5h of (Dessart, Hillier, & Audit 2017). The inset shows a close-up of the region of Na I D absorption in the spectrum of SN 2018zd at $t \approx 5$ d. (b) Photospheric-phase spectra of SN 2018zd along with those of SN 1998S, SN 1999em (Hamuy et al. 2001; Leonard et al. 2002), SN 2005cs (Pastorello et al. 2006), SN 2013by, SN 2013ej (Dhungana et al. 2016), and 2013 SN 2013fs. (c) Three nebular-phase spectra of SN 2018zd (at 250 d, 338 d, and 399 d) compared with model spectra corresponding to different progenitor masses (Jerkstrand et al. 2012; 12 M $_{\odot}$ at 250 d, 306 d, and 400 d; 15 M $_{\odot}$ at 250 d, 332 d, and 400 d; and 19 M $_{\odot}$ at 250 d, 332 d, and 369 d). The model spectra are scaled to the distance of SN 2018zd and its ^{56}Ni mass. The inset shows the velocity distribution of the H α emission of SN 2018zd at $t = 182$ d, 250 d, 338 d, and 399 d; the instrumental resolution was removed via $\text{FWHM}_{\text{corr}} = (\text{FWHM}_{\text{obs}}^2 - \text{FWHM}_{\text{inst}}^2)^{1/2}$, where the instrumental FWHM was measured from the night-sky emission lines. In panels (a) and (c), dashed lines mark spectral features at rest; in panel (b), dotted lines indicate spectral features at $v = -3500$ km s $^{-1}$. In panels (a) and (b), residuals from incomplete removal of telluric absorption are marked with an Earth symbol. The host-galaxy redshift and the extinction from the host galaxy and the Milky Way have been removed.

of SN 2013fs and SN 1998S in mass immediately before the explosion.

4.2 Photospheric phase

Panel (b) of Fig. 8 displays spectra of SN 2018zd from $t \approx 12$ d to $t \approx 68$ d compared with photospheric-phase spectra of SNe 1999em and 2005cs, as well as with spectra of SNe 1998S, 2013by, 2013ej, and 2013fs at similar epochs.

At this phase, spectra of SN 2018zd are still characterised by a featureless blue continuum, likely due to continuous heating by CSM interaction. Consequently, the spectrum of SN 2018zd at $t \approx 12$ d looks younger than that of SN 2005cs at $t \approx 3$ d and SN 1999em at $t \approx 4$ d; it has a bluer colour and a weaker P-Cygni $H\alpha$ profile. Given its blue and featureless spectrum, SN 2018zd might be classified as a very young SN II (e.g., 1–2 d after the explosion) if it had not been spectrally observed until $t \approx 12$ d. Moreover, cross-correlation with a library of SN spectra using the supernova identification code (SNID; Blondin & Tonry 2007) shows that spectra of SN 2018zd at $t \approx 23$, 43, and 68 d respectively match those of SN 2005cs at $t \approx 4$, 10, and 13 d, SN 1999em at $t \approx 6$, 11, and 33 d, and SN 2004et at $t \approx 7$, 9, and 40 d.

Khazov et al. (2016) reported that 14% of their SN II sample observed at $t < 10$ d show flash spectral features. This fraction might be underestimated because interaction makes SNe II look somewhat younger than their real age. For example, SN 2018zd might have been counted as a young SN II without flash features if both the discovery date and classification date had been delayed by ~ 10 d.

At $t \approx 13$ d, the spectrum of SN 2018zd looks similar to that of SN 1998S at a comparable phase, but it shows a more pronounced P-Cygni profile of the $H\alpha$ line than the latter. The spectrum of SN 2013fs at $t \approx 13$ d exhibits a redder continuum and more noticeable Balmer lines than that of SN 2018zd, suggesting short-lived contribution of ionisation/interaction in the former, as seen in the flash phase.

The evolution in the light curve, surface radius, and temperature indicate that SN 2018zd starts recombination at $t \approx 40$ d. After this phase, the spectrum of SN 2018zd (e.g., $t \approx 43$ d) evolves to be like that of SNe IIP. For example, the spectrum of SN 2018zd at $t \approx 68$ d is somewhat similar to that of SN 1999em at $t \approx 40$ d, but with narrower and shallower spectral features. The contribution of CSM interaction still exists ~ 2 months after the explosion, as suggested by the bluer $uvw2 - u$ and $B - V$ colours of SN 2018zd at the same phase.

The EW ratio between the blue absorption wing and red emission wing of $H\alpha$ in spectra of SN 2018zd ($R_{H\alpha} \approx 0.3$) is smaller than that of SN 1999em ($R_{H\alpha} \approx 0.6$) but larger than that of SN 2013by ($R_{H\alpha} \approx 0.1$), at $t \approx 20 - 30$ d. SN 1998S does not show a well-developed $H\alpha$ absorption component at $t \approx 71$ d ($R_{H\alpha} < 0.1$). The relatively weak $H\alpha$ absorption of SN 2013by and SN 19998S is usually seen in other SNe IIL (Schlegel 1996). The narrower $H\alpha$ profile and the lower $R_{H\alpha}$ of SN 2018zd might be related to a slower bulk expansion velocity than that of typical SNe IIP (Dessart et al. 2009). It is consistent with the low expansion velocity of SN 2018zd seen in Section 5.1 and 5.3.

4.3 Nebular phase

In the nebular phase, spectra of SN 2018zd evolve to be more like that of a normal SN IIP, dominated by emission lines of [O I], $H\alpha$, [Fe II], [Ca II], and Ca II. Panel (c) of Fig. 8 shows three nebular spectra of SN 2018zd and model spectra of different progenitor masses (Jerkstrand et al. 2012). Comparison of the strength of [O I] $\lambda\lambda 6300, 6364$ between the observation and model suggests that the progenitor mass of SN 2018zd is in the range from $12 M_{\odot}$ to $15 M_{\odot}$, but preferring a lower mass.

The inset panel shows a close-up view of the $H\alpha$ emission; the profile of has been corrected for the instrumental broadening effect, $\text{FWHM}_{\text{corr}} = (\text{FWHM}_{\text{obs}}^2 - \text{FWHM}_{\text{inst}}^2)^{1/2}$, where FWHM_{obs} is the observed full width at half-maximum intensity (FWHM), and $\text{FWHM}_{\text{inst}}$ is the instrumental FWHM. This emission becomes progressively narrower from $t \approx 182$ d to $t \approx 338$ d, and then it levels off. The asymmetric $H\alpha$ emission at $t \approx 399$ d might imply an asymmetric structure in the inner part of this SN.

Maguire et al. (2012) reported a relation that can be roughly used to estimate the ^{56}Ni mass from $\text{FWHM}_{\text{corr}}$: $M(^{56}\text{Ni}) = A \times 10^{B \times \text{FWHM}_{\text{corr}}} M_{\odot}$, where $B = 0.233 \pm 0.0041$ and $A = 1.81^{+1.05}_{-0.68} \times 10^{-3}$. The $\text{FWHM}_{\text{corr}}$ of SN 2018zd at $t \approx 399$ d is measured to be $54.2 \pm 1.0 \text{ \AA}$, which yields $M(^{56}\text{Ni}) = 0.033 \pm 0.004 M_{\odot}$. This estimate is consistent with the value derived from the light-curve tail (see Section 5.2).

5 DISCUSSION

5.1 Ejecta velocities

The ejecta velocities of SN 2018zd measured from the absorption minima (including $H\alpha$, $H\beta$, Fe II $\lambda 5018$, Fe II $\lambda 5169$, Sc II $\lambda 6246$, Si II $\lambda 6355$, and Ca II $\lambda 8662$) and the expanded photospheric radius are presented in the top panel of Fig. 9. For comparison, the ejecta velocities of SNe 1999em, 1998S, 2005cs, and 2016bkv derived from absorption minima of $H\alpha$ and Fe II $\lambda 5169$ are plotted in the bottom panel.

The velocity derived from the expanding photospheric radius of SN 2018zd ($v = \Delta R / \Delta t$) is $\sim 1000 \text{ km s}^{-1}$ at $t \approx 4$ d, which accelerates at an average of $1200 \text{ km s}^{-1} \text{ d}^{-1}$ in the next five days. It reaches the maximum velocity ($\sim 8000 \text{ km s}^{-1}$) at $t \approx 8.8$ d when the bolometric luminosity rose to the peak. This velocity decreases quickly during the next week and reaches a velocity plateau at $\sim 3600 \text{ km s}^{-1}$. The acceleration inferred from the photospheric radius might relate to the surrounding density structure of the SN. A CSM cloud with a density profile increasing outward may absorb progressively more energy from the shock, resulting in a fast-rising luminosity curve that may mimic an accelerating expansion of the photosphere.

The remarkable acceleration is seen in the velocity derived from the absorption minima of $H\alpha$ and $H\beta$ of SN 2018zd at $t \lesssim 20$ d. At the same phase, the $H\alpha$ velocity of SN 2016bkv shows a similar increase, as noted by Nakaoka et al. (2018). This acceleration might imply distinct line-forming regions. At early phases, the weak H absorption forms in the wind/CSM that is above the optically-thick photosphere. The shocked ejecta ionise and accelerate this material to yield the observed spectral lines and acceleration. The H absorption lines in the well-developed P-Cygni

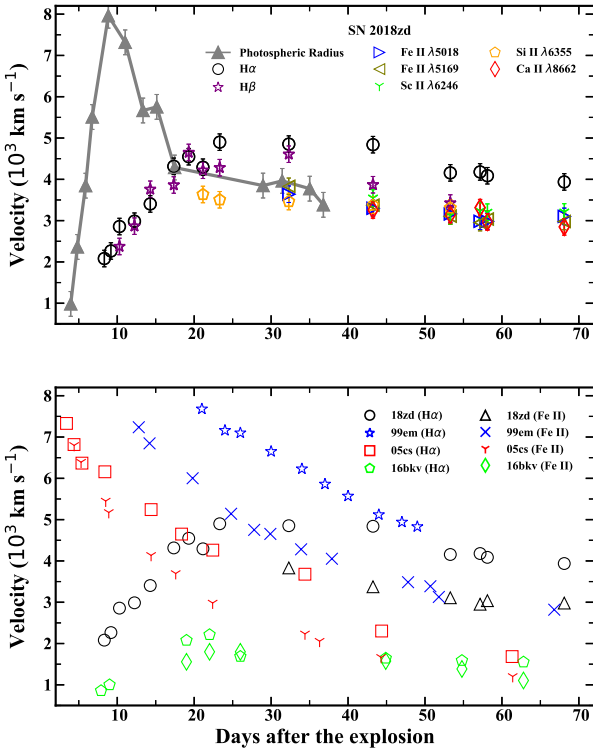


Figure 9. *Top:* Ejecta velocity of SN 2018zd derived from the absorption minima of $H\alpha$, $H\beta$, $\text{Fe II } \lambda 5018$, $\text{Fe II } \lambda 5169$, $\text{Sc II } \lambda 6246$, $\text{Si II } \lambda 6355$, and $\text{Ca II } \lambda 8662$. The velocity derived from the photospheric radius presented in Fig. 7 is also plotted. *Bottom:* Ejecta velocity of SNe 2018zd, 1999em, 2005cs, and 2016bkv derived from the absorption minima of $H\alpha$ and $\text{Fe II } \lambda 5169$. The uncertainty is about $200\text{--}300 \text{ km s}^{-1}$.

profile at $t > 20 \text{ d}$ form in the ejecta that decelerate owing to obstruction by the outer material.

At $t > 20 \text{ d}$, some well-developed absorptions can be used to estimate the velocity of SN 2018zd besides of the H lines. The velocity derived from those absorptions at $t \approx 30 \text{ d}$ is close to that from the photospheric radius but is $\sim 1000 \text{ km s}^{-1}$ slower than that from H lines. As usually seen in the normal SNe IIP, the velocity derived from H lines is higher than those from the other ions (Leonard et al. 2002). Considering these differences, we use $\text{Fe II } \lambda 5169$ and $\text{Sc II } \lambda 6246$ as the tracker of photospheric velocity instead of H lines, as suggested by Hamuy (2003) and Maguire et al. (2010). The velocity of SN 2018zd at $t = 50 \text{ d}$ interpolated by the velocity of $\text{Fe II } \lambda 5169$ and $\text{Sc II } \lambda 6246$ is about 3300 km s^{-1} , which is at the slow side of normal SNe IIP (as seen in Section 5.3) and is faster than the low-velocity SNe IIP (e.g., SN 2005cs).

5.2 Bolometric flux and explosion parameters

Fig. 10 displays the bolometric light curve of SN 2018zd based on the SED presented in Section 3.5. The flux at wavelengths redder than the photometry is derived by extrapolating a blackbody fit to the SED. The flux at wavelengths shorter than 1216 \AA is assumed to be zero because of absorption in the H-rich atmosphere (Lyman series). At $t < 115 \text{ d}$, when UV photometry is available, we extrapolate the $uvw2$

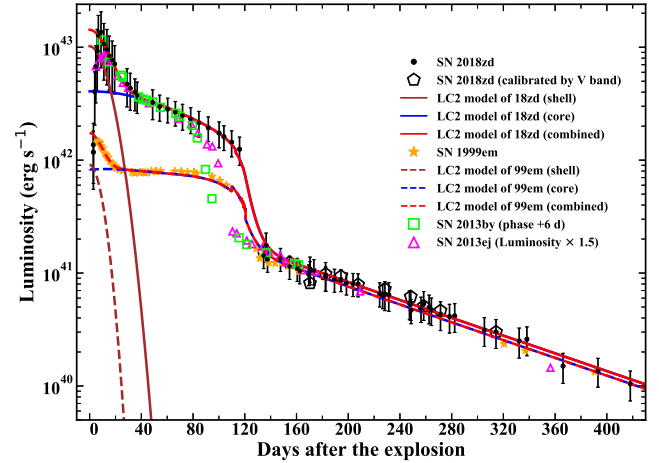


Figure 10. Bolometric light curve of SN 2018zd compared with that of SN 1999em, SN 2013by, SN 2013ej and the results of the LC2 model. The error bars include uncertainties in the photometry, extinction, and distance, the last two of which greatly dominate. The LC2 model contains the contribution of the core and the shell. The phase of SN 2013by has been shifted by +6 d corresponding to the archival explosion date (MJD = 56403.5; Valenti et al. 2015). The luminosity of SN 2013ej has been multiplied by 1.5.

band (or the $uvw2$ band if $uvw2 - u \gtrsim 1.0 \text{ mag}$ to avoid the red leak of the $uvw2$ band; Brown et al. 2016) flux using a straight line to zero flux at 1216 \AA (as seen in Fig. 7). In the tail phase, we omit the flux at wavelengths shorter than 3600 \AA and extrapolate the flux beyond the wavelength range covered by the photometry via the blackbody directly. The latter treatment yields a luminosity match to that derived using the V -band photometry via the equation (Bersten & Hamuy 2009)¹⁰ during $135 \text{ d} \lesssim t \lesssim 338 \text{ d}$:

$$\log L = -0.4[BC + V - A_V + 11.64] + \log(4\pi D^2), \quad (1)$$

where L is given in units of erg s^{-1} , the colour term $BC = -0.7 \text{ mag}$, and D is the SN distance in units of cm.

The bolometric light curves of SN 1999em, SN 2013by, and SN 2013ej produced by the same method, and the bolometric light curve generated by the two-component model (LC2) of Nagy & Vinkó (2016), are also shown for comparison. LC2 is a semianalytical light-curve model, which computes the bolometric light curve of a homologous expanding supernova using the radiative diffusion approximation as introduced by Arnett & Fu (1989).

SN 2018zd reached its bolometric peak at $t \approx 8.8 \text{ d}$, $L_{\text{max}} = (1.36 \pm 0.63) \times 10^{43} \text{ erg s}^{-1}$, higher than that of SN 1999em by a factor of eight, as listed in Table 2. The large peak luminosity of SN 2018zd is partly due to the contribution of interaction between the shocked ejecta and stellar wind/CSM. This SN reached UV and optical maxima almost simultaneously, which also helped explain the higher peak bolometric luminosity. At the tail phase ($t \gtrsim 130 \text{ d}$), however, these two SNe are found to have similar luminos-

¹⁰ The “ -11.64 ” in Equation 4 of Bersten & Hamuy (2009) is altered to be “ $+11.64$ ” to correct the typo.

Table 2. Parameters of bolometric light curves^a

Supernova	Distance (Mpc)	E(B-V) _{total}	$L_{\text{peak}}(10^{43}\text{ergs}^{-1})$	$M(^{56}\text{Ni})(M_{\odot})^b$	Explosion date (MJD)	Ref. ^c
SN 2018zd	18.4 (4.5)	0.17 (0.05)	1.36 (0.63)	0.035 (0.012)	58178.4 (0.5)	1
SN 1999em	8.2 (0.6)	0.10 (0.05)	0.15 (0.03)	0.033 (0.006)	51475.1 (1.4)	2
SN 2013by	14.8 (1.0)	0.20 (0.03)	1.15 (0.24)	0.036 (0.006)	56397.5 (2.0)	3,1
SN 2013ej	9.6 (0.7)	0.10 (0.03)	0.57 (0.08)	0.024 (0.005)	56496.5 (1.5)	4

^aThe parameters in Fig. 10. The number given in the brackets are the 1σ uncertainties. ^bMass of ^{56}Ni derived by the bolometric luminosity during $130\text{ d} \lesssim t \lesssim 180\text{ d}$ via Eq. 2. ^cReference of the distance, reddening and explosion date adopted in the calculation: 1. This work, 2. Leonard et al. (2002), 3. Valenti et al. (2015), 4. Huang et al. (2015).

ity ($L \approx 1.2 \times 10^{41}\text{ ergs}^{-1}$ at $t \approx 150\text{ d}$) and decline rate ($\sim 0.98\text{ mag } 100\text{ d}^{-1}$, as expected from Co \rightarrow Fe decay).

The expansion velocity of SN 2018zd matches that of SN 1999em within $\sim 200\text{ km s}^{-1}$ at $t \approx 50\text{ d}$, as presented in Fig. 9. They are expected to have a similar middle plateau luminosity at a statistical uncertainty of 0.5 mag if they follow the velocity-luminosity relation (Hamuy 2003), as seen in panel (a) of Fig. 11. Moreover, SN 2018zd exhibits a tail similar to that of SN 1999em after the contribution of CSM interaction disappeared. Thus, it might be reasonable to assume that the energy produced in the explosion of SN 2018zd is close to that of SN 1999em at the uncertain level of the velocity-luminosity relation if the former has no extra energy input from the interaction. Assuming all of the excess emission inferred in SN 2018zd relative to that of SN 1999em is converted from the kinetic energy of the ejecta ($M_{\text{wind}} = \int_3^{120} [L_{18\text{zd}}(t) - L_{99\text{em}}(t)]/v_{\text{ej}}^2(t) dt$, where the photospheric ejecta velocity $v_{\text{ej}}(t)$ is derived from the absorption minimum of Fe II lines, as presented in Fig. 9; $v_{\text{ej}}(t)$ at $t > 70\text{ d}$ is set to 3300 km s^{-1} , the integration limit is from the first date when SN 2018zd having multi-band photometry to the end of plateau phase), we find that $0.18_{-0.10}^{+0.05} M_{\odot}$ of wind material is required to produce the extra flux seen in SN 2018zd. The uncertainty in the wind-mass estimate includes the uncertainties in bolometric flux and the velocity-luminosity relation. This stellar wind is more massive than that of SN 2013fs ($\lesssim 0.01 M_{\odot}$; estimated via the line luminosity of the narrow H α emission in Yaron et al. 2017, and spectral modeling in Dessart, Hillier, & Audit 2017) but less massive than that of SN 1998S ($\sim 0.4 M_{\odot}$; derived from spectral modeling in Dessart et al. 2016).

SN 2013by shows a bolometric light curve similar to that of SN 2018zd at $t \lesssim 80\text{ d}$ if its epoch is shifted by +6 d. Given that the closest available prediscovery image of SN 2013by is about 22 d earlier than the discovery image (Parker et al. 2013) it is possible that SN 2013by exploded a few days earlier than the explosion date reported by Valenti et al. (2015). Thus, we adopt MJD = 56397.5 as the explosion date of SN 2013by for the following calculation. With this modified explosion date, the colour curve and light curve of SN 2013by matches that of SN 2018zd better. At $t > 80\text{ d}$, SN 2013by ends the plateau phase and fades quickly. However, its tail luminosity meets that of SN 2018zd again.

The bolometric light curve of SN 2013ej roughly matches that of SN 2018zd and SN 2013by except the middle part ($80\text{ d} \lesssim t \lesssim 120\text{ d}$) if the luminosity of SN 2013ej is multiplied by 1.5. These three SNe show a faster-declining

Table 3. LC2 model parameters of SN 2018zd and SN 1999em^a

Parameter	SN 2018zd		SN 1999em	
	“core”	“shell”	“core”	“shell”
Initial	model	parameters		
R_0 (10^{13} cm)	4.8	7.0	3.5	5.0
M_{ej} (M_{\odot})	9.80	0.55	13.50	0.20
M_{Ni} (M_{\odot})	0.033	0	0.030	0
T_{rec} (K)	6000	0	7000	0
E_{kin} (10^{51} erg)	2.20	1.30	1.48	0.40
E_{th} (10^{51} erg)	1.90	0.40	0.40	0.02
α	1.6	0.0	0.0	0.0
κ ($\text{cm}^2\text{ g}^{-1}$)	0.28	0.40	0.26	0.40
Calculated	physical	properties		
t_0 (d)	95.6	18.7	102.9	11.7
v (km s^{-1})	6580	23200	4290	21300

^a R_0 is the initial radius of the ejecta, M_{ej} is the ejected mass, M_{Ni} is the initial nickel mass, T_{rec} is the recombination temperature, E_{kin} is initial kinetic energy, E_{th} is the initial thermal energy, α is the density profile exponent, κ is the opacity, t_0 is the light-curve timescale, and v is the maximum expansion velocity.

plateau and a more significant drop from the plateau to the radioactive tail than does SN 1999em.

We estimate the mass of ^{56}Ni ejected by the SN based on the tail bolometric luminosity via (Hamuy 2003):

$$M_{\text{Ni}} = (7.866 \times 10^{-44}) L_t \times \exp\left[\frac{t/(1+z) - 6.1}{111.26}\right] M_{\odot}, \quad (2)$$

where t is the phase after explosion, L_t is the tail-phase luminosity in units of ergs^{-1} , and z is the redshift of the SN. SN 2018zd, SN 1999em, and SN 2013by produced similar amounts of ^{56}Ni , as listed in Table 2, given the similar radioactive tails.

It is not surprising to see that the mass of ^{56}Ni derived by the LC2 model, $0.033 M_{\odot}$, is consistent with the above results, because they rely on a shared physical basis (Arnett 1982; Arnett & Fu 1989). Thus, the mean value of $M(^{56}\text{Ni})$ derived via the tail-phase flux matches the result from the nebular spectra. Since the estimate from the nebular spectra is relies only on the FWHM of H α emission, which is independent of distance and extinction, the agreement between these two methods suggests that the distance and extinction of SN 2018zd adopted in this paper are reasonable.

The LC2 model reproduces the light curve of SN 1999em and also the light curve of SN 2018zd at $t \gtrsim 10\text{ d}$ with the

parameters listed in Table 3. Note that all models shown are not from formal fitting to the data. Instead, they can be considered only as representative examples that look similar to the observations. Thus, formal uncertainties cannot be assigned to the parameters shown in Table 3, but they are at least ~ 10 per cent according to Nagy & Vinkó (2016).

The velocity derived in the LC2 model is about 2000 km s^{-1} higher than that of SN 2018zd obtained from the spectral features, as presented in Section 5.1. This suggests that extra energy is required to produce such a luminous SN in the scheme of regular SNe IIP. A significant amount of the SN kinetic energy may be converted to thermal energy via the CSM interaction, conforming to the high temperature seen in Fig. 7.

5.3 Comparison with other SNe II

Fig. 11 displays the position of SN 2018zd in the spectroscopic and photometric parameter space of SNe II. Comparing with the linear fitting in each panel, we note the following:

(1) The peak (M_{max}) and middle plateau (M_V^{50}) of SN 2018zd are (respectively) 1.50 ± 0.75 mag and 1.75 ± 0.53 mag brighter than the sample SNe having a similar decline rate s_2 (Anderson et al. 2014) and ejecta expansion velocity (v_{exp}^{50}) in panels (a) and (c).

(2) SN 2018zd experienced a significant luminosity drop from the peak to the tail, a $\sim 2\sigma$ departure from the linear fitting of M_{max} vs. M_{tail} in panel (e).

(3) The tail brightness of SN 2018zd follows that of the SN II family. For example, the mass of synthesised ^{56}Ni in SN 2018zd matches the v_{exp}^{50} vs. $M(^{56}\text{Ni})$ relation in panel (b), and the brightness at the beginning of the tail phase is located in the 1σ region of s_2 vs. M_{end} space in panel (d).

Two other SNe II, SN 2013ej and SN 2013by, show somewhat similar behaviour not only in bolometric light curves but also their positions in the SN II family. They have an intermediate flux drop during the transition from the plateau to the radioactive tail, smaller than that of SN 2018zd but more significant than the sample cluster. Combined with their fast light-curve decline rate during the photospheric phase, these two SNe might have extra energy injected by CSM interaction. Valenti et al. (2015) also suggest that the interaction scenario explains the fast-declining light curves of SN 2013by based on the flash spectral features in the spectrum at $t \approx 2$ d (as seen in Fig. 8) and the detection of the X-ray emission. Moreover, Morozova, Piro, & Valenti (2017) use a dense wind-like CSM interaction model to produce the luminous and fast-declining light curve of SN 2013ej and SN 2013by. The brightness of SN 2013ej and SN 2013by in the middle of the plateau phase follows the velocity-luminosity relation of SNe IIP, as seen in the panel (a) of Fig. 11. It seems that the extra energy in these two SNe disappeared at $t \approx 50$ d, which suggests an interaction lasting for a period shorter than that of SN 2018zd.

SN 2018zd is an outlier in velocity-brightness space, as seen in panel (a). However, a group of luminous SNe with low expansion velocities (LLEV SNe; Rodríguez et al. 2020)

is located in a more distant region relative to the bulk of sample than SN 2018zd. The middle plateau brightness of the LLEV SNe is ~ 2 – 3 mag brighter than that of SNe II having the same ejecta expansion velocity. A larger drop from the peak to the tail in the light curve is also found in the LLEV SNe. Rodríguez et al. (2020) listed the observational characteristics of the LLEV SNe that are also found in SN 2018zd, such as the ejecta-CSM interaction signs at early phases, blue $B - V$ colours, weakness of metal lines, and luminous peak and plateau compared with the low expansion velocities. All of these properties were reproduced, assuming ejecta-CSM interaction that lasts between 4 and 11 weeks post-explosion, in the model work of Rodríguez et al. (2020). It confirms the interaction scenario of SN 2018zd suggested by our analysis here.

5.4 Electron-capture supernova

The typical temperature of the shocked CSM is $\sim 10^9$ K and that of the shocked ejecta is $\geq 10^7$ K, and both radiate in the X-ray band (Branch & Wheeler 2017). These X-ray photons ionise the atoms in the surrounding wind/CSM, which then radiate narrow emission lines in the UV-optical band (i.e., the flashed spectral features) owing to recombination. Thus, we expect to detect the X-rays from SNe II if this radiation is not strongly absorbed by the unshocked material. However, Chandra, Chevalier, & Fransson (2018) reported the non-detection of SN 2018zd with the *Swift* X-ray telescope (XRT) between March 04 and March 11, 2018. They found an upper flux limit of $5.22 \times 10^{-14} \text{ erg cm}^2 \text{ s}^{-1}$ (0.3–10 keV). Adopting $D = 18.4$ Mpc, the upper limit for the X-ray luminosity of SN 2018zd is $\sim 2.11 \times 10^{39} \text{ erg s}^{-1}$, slightly less than the detected luminosity of SN 2013by ($\sim 2.88 \times 10^{39} \text{ erg s}^{-1}$; Valenti et al. 2015). The weaker X-ray radiation of SN 2018zd than that of SN 2013by might be related to the stronger flash emission features of the former. It is possible that the majority of the X-ray photons from the shocked material are absorbed by the wind/CSM, producing stronger emission lines in the optical spectra.

Moriya et al. (2014) suggested that the optically bright but X-ray-faint SNe IIn can arise from electron-capture supernovae (ECSNe) that is exploded from the super-asymptotic giant branch (super-AGB) star (Miyaji et al. 1980; Nomoto et al. 1982; Miyaji & Nomoto 1987). Super-AGB stars have a dense and massive circumstellar environment due to its high mass-loss rate wind, which could create narrow emission lines during the SN explosion, as seen in SN 2018zd. ECSNe is possible to be as luminous as SNe IIn at the peak phase due to the larger radius of the progenitor star, but the tail is faint because of the intrinsic low explosion energy and a small amount of ^{56}Ni (Tominaga, Blinnikov & Nomoto 2013; Moriya et al. 2014). The synthesised mass of ^{56}Ni in SN 2018zd is relatively small compared to its luminous peak. Furthermore, this SN produced even less ^{56}Ni if a shorter distance is adopted in the calculation. For example, it yields only $0.013 \pm 0.004 M_{\odot}$ if $D = 11.3 \pm 2.0$ Mpc (Bottinelli et al. 1984), which is close to the upper limit mass of ^{56}Ni produced in ECSNe ($< 0.015 M_{\odot}$; Kitaura, Janka & Hillebrandt 2006).

Thus, given the luminous UV-optical peak, the relatively weak X-ray radiation, the massive wind/CSM environment, and a relatively small amount of synthesised ^{56}Ni ,

the electron-capture triggered supernova explosion is also a possible scenario of SN 2018zd.

6 CONCLUSIONS

We present an extensive set of observations of SN 2018zd from the early “flash-ionisation” spectroscopic phase (e.g., $t \lesssim 1$ d) to the later nebular phase (e.g., $t \approx 456$ d). The flux excess observed in the clear-band light curve ~ 3.6 hr after the explosion might be a signal of shock breakout. The overluminous peak [e.g., $L_{\max} = (1.36 \pm 0.62) \times 10^{43} \text{ erg s}^{-1}$] of this SN accompanied by flash spectra at early times is likely caused by extra energy injection via interaction between the shocked ejecta and the massive wind ($0.18^{+0.05}_{-0.10} M_{\odot}$). This effect does not disappear immediately when the flash signatures in the spectra fade away. Energy is stored in the H-rich envelope and heats it, making SN 2018zd bluer than regular SNe IIP, as seen in its colour curve and spectrum during the photospheric phase. Meanwhile, this energy makes a brighter mid-plateau for SN 2018zd than regular SNe II having the same expansion velocity. SN 2018zd is thus a gap-filler event between the central cluster and separated LLEV SNe in velocity-brightness space, perhaps implying a continuous distribution of the interaction contribution. Given the similar fast-declining light curve of SNe II reported by Huang et al. (2015) for SN 2013ej and Valenti et al. (2015) for SN 2013by, there is a group of transitional events located at the boundary between SNe IIP and SNe IIL in the sense of decline rate. Finally, the nebular spectra and the light-curve tail of SN 2018zd resemble those of typical SNe IIP when the injected energy has been released. Thus, the observations of SN 2018zd presented in this paper are key to understanding the nature of the diverse origins of SNe II.

ACKNOWLEDGEMENTS

An anonymous referee made many useful suggestions that improved this paper. We acknowledge the support of the staff of the LJT, TNT, XLT, KOT, WT, and Keck. Funding for the LJT has been provided by the CAS and the People’s Government of Yunnan Province. The LJT is jointly operated and administrated by YNAO and Center for Astronomical Mega-Science, CAS. Some of the data presented herein were obtained at the W. M. Keck Observatory, which is operated as a scientific partnership among the California Institute of Technology, the University of California, and NASA; the Observatory was made possible by the generous financial support of the W. M. Keck Foundation. We are grateful for discussions with Luc Dessart, Osmar Rodríguez, Mario Hamuy, Peter Brown, Paolo Mazzali, and Pina Elena about this work.

J.Z. is supported by the National Natural Science Foundation of China (NSFC, grants 11773067, 11403096), by the Western Light Youth Project, and by the Youth Innovation Promotion Association of the CAS (grant 2018081). This work is sponsored (in part) by the CAS South America Center for Astronomy (CASSACA) in Santiago, Chile. X.W. is supported by NSFC (grants 11633002 and 11761141001) and the Major State Basic Research Development Program

(grant 2016YFA0400803). J.V. and his group at Konkoly Observatory are supported by the project “Transient Astrophysical Objects” GINOP 2.3.2-15-2016-00033 of the National Research, Development and Innovation Office (NKFIH), Hungary, funded by the European Union. R.K.-T. is also supported by the ÚNKP-19-02 New National Excellence Program of the Ministry for Innovation and Technology. L.W. acknowledges support from the the Polish NCN DAINA grant 2017/27/L/ST9/03221 and EC’s H2020 OPTICON grant 730890. A.V.F.’s supernova group is grateful for financial assistance from the Christopher R. Redlich Fund, the TABASGO Foundation, and the Miller Institute for Basic Research in Science (U.C. Berkeley). P.M. acknowledges support provided by the Polish National Science Center (NCN) through grant 2016/21/B/ST9/01126. We acknowledge the Gaia Photometric Alerts group and the use of the Cambridge Photometric Calibration Server (<http://gsaweb.ast.cam.ac.uk/followup>), developed by Sergey Koposov and maintained by Lukasz Wyrzykowski, Arancha Delgado, and Pawel Zielinski, funded by the European Union’s Horizon 2020 research and innovation programmer under grant agreement 730890 (OPTICON). K.V. and L.K. are grateful for financial support from the National Research, Development and Innovation Office (NKFIH), Hungary, under grants NKFI-K-131508 and NKFI-KH-130526. Á.S., A.B., C.K., and K.V. are supported by the Lendület program grant LP2018-7/2019 of the Hungarian Academy of Sciences.

REFERENCES

- Adamo, A., Smith, L. J., Gallagher, J. S., et al. 2012, MNRAS, 426, 1185
- Anderson, J. P., Conzález-Gaitán, S., Hamuy, M., et al. 2014, ApJ, 786, 67
- Arcavi, I., Gal-Yam, A., Cenko, S. B., et al. 2012, ApJL, 756, L30
- Arnett, W. D. 1982, ApJ, 253, 786
- Arnett, W. D., & Fu, A. 1989, ApJ, 340, 396
- Bersten, M., & Hamuy, M., 2009, ApJ, 701, 200
- Blondin, S., & Tonry, J. 2007, ApJ, 666, 1024
- Bottinelli, L., Gouguenheim, L., Paturol, G., et al. 1984, A&A, 56, 381
- Branch, D., & Wheeler, J. C. 2017, in Supernova Explosions (Springer), Chapter 6
- Brown, P., Breeveld, A., Roming, P., et al. 2016, AJ, 152, 102
- Bullivant, C., Smith, N., Williams, G. G., et al. 2018, MNRAS, 476, 1497
- Chandra, P., Chevalier R. A., & Fransson, C. 2018, ATel. #11405
- Danziger, I. J. 1988, Sky and Telescope, 75, 611
- Dessart, L., Hillier, D. J., & Audit, E. 2017, A&A, 605, 83
- Dessart, L., Hillier, D. J., Waldman, R., et al. 2013, MNRAS, 433, 1745
- Dessart, L., Hillier, D. J., Audit, E., et al. 2016, MNRAS, 458, 2094
- Dessart, L., Hillier, D. J., Gezari, S., et al. 2009, MNRAS, 394, 21
- Dhungana, G., Kehoe, R., Vinkó, J., et al. 2016, ApJ, 822, 6
- Elhamdi, A., Danziger, I. J., Chugai, N., et al. 2003, MNRAS, 338, 939
- Fan, Y.-F., Bai, J.-M., Zhang, J.-J., et al. 2015, RAA, 15, 918
- Faran, T., Poznanski, D., Filippenko, A.V., et al. 2014, MNRAS, 445, 554
- Fassia, A., Meikle, W. P. S., Chugai, N., et al. 2001, MNRAS, 325, 907

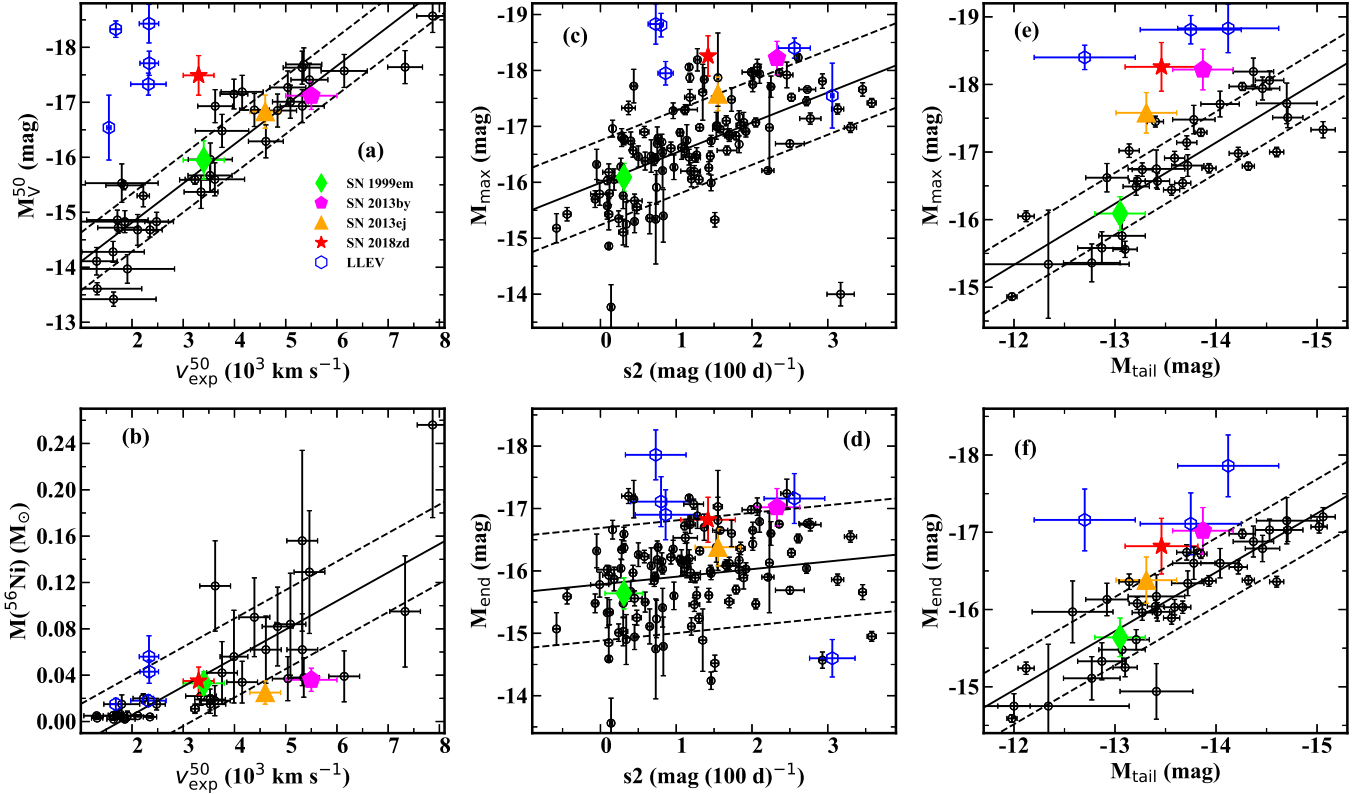


Figure 11. The position of SN 1818zd in the SN II family considering various photometric and spectroscopic indicators, including the velocity of Sc II $\lambda 6246$ or Fe II $\lambda 5169$ measured at $t \approx 50$ d after explosion (i.e., v_{exp}^{50}), the V-band absolute magnitude measured at $t \approx 50$ d after explosion (i.e., M_V^{50}), the mass of ^{56}Ni (i.e., $M(^{56}\text{Ni})$), and four shape parameters of the V-band light curve (as defined by Anderson et al. 2014) — the absolute brightness at three selected phases (i.e., M_{max} , M_{end} , and M_{tail}) and the decline rate of the plateau (i.e., s_2). The solid lines are the linear fits to black open circles (collected from Hamuy 2003; Anderson et al. 2014; Spiro et al. 2014; Zhang et al. 2014), and the dashed lines are the 1σ uncertainties of the linear fits. SN 1999em, SN 2013ej, SN 2013by, and five luminous SNe with low expansion velocities (LLEV SNe; Rodríguez et al. 2020) are included for comparison.

Fassia, A., Meikle, W. P. S., Vacca, W. D., et al. 2000, MNRAS, 318, 1093
 Filippenko, A. V. 1982, PASP, 94, 715
 Filippenko, A. V. 1988, AJ, 96, 1941
 Filippenko, A. V. 1997, ARAA, 35, 309
 Filippenko, A. V., Matheson, T., & Ho, L. C. 1993, ApJ, 415, L103
 Fransson, C., Ergon, M., Challis, P. J., et al. 2014, ApJ, 797, 118
 Gal-Yam, A. 2017, in Handbook of Supernovae (Springer), 195
 Gal-Yam, A., Arcavi, I., Ofek, E. O., et al. 2014, Nature, 509, 471
 Garnavich, P. M., Tucker, B. E., Rest, A., et al. 2016, ApJ, 820, 23
 Gehrels, N., Chincarini, G., Giommi, P. et al. 2004, ApJ, 611, 1005
 Giraud, E. 1985, A&A, 153, 125
 Grassberg, E. K., & Nadyozhin, D. K. 1976, Ap&SS, 44, 409
 Hamuy, M. 2001, Ph.D. thesis, Univ. Arizona
 Hamuy, M. 2003, ApJ, 582, 905
 Hamuy, M., Pinto, P. A., Maza, J., et al. 2001, ApJ, 558, 615
 Hosseinzadeh, G., Valenti, S., McCully, C., et al. 2018, ApJ, 861, 63
 Huang, F., Li, J. Z., Wang, X. F., et al. 2012, RAA, 11, 1585
 Huang, F., Wang, X. F., Zhang, J. J., et al. 2015, ApJ, 807, 59
 Jerkstrand, A., Ertl, T., Janka, H.-T., et al. 2018, MNRAS, 475, 277
 Jerkstrand, A., Fransson, C., Maguire, K., et al. 2012, A&A, 546,

28
 Khazov, D., Yaron, O., Gal-Yam, A., et al. 2016, ApJ, 818, 3
 Kitaura F. S., Janka H.-T., & Hillebrandt W., 2006, A&A, 450, 345
 Krisciunas, K., Hamuy, M., Suntzeff, N.B., et al. 2009, ApJ, 137, 34
 Landolt, A. V. 1992, AJ, 104, 340
 Leonard, D. C., Filippenko A. V., Barth, A. J., et al. 2000, ApJ, 536, 239
 Leonard, D. C., Filippenko, A. V., Gates, E. L., et al. 2002, PASP, 114, 305
 Li, W., Leaman, J., Chornock, R., et al. 2011, MNRAS, 412, 1441
 Maguire, K., DiCarlo, E., Smartt, S. J., et al. 2010, MNRAS, 404, 981
 Mikolajczyk, P., & Wyrzykowski, L. 2018, ATel. #12079
 Misra, K., Pooley, D., Chandra P., et al. 2007, MNRAS, 381, 280
 Miyaji, S., Nomoto, K., Yokoi, K., & Sugimoto, D. 1980, PASJ, 32, 303
 Miyaji, S., & Nomoto, K. 1987, ApJ, 318, 307
 Moriya, T. J., Tominaga, N., Langer, N., et al. 2014, A&A, 569, 57
 Morozova, V., Piro, A. L., & Valenti, S., et al. 2017, ApJ, 838, 28
 Mould, J. R., Huchra, J. P., Freedman, W. L., et al. 2000, ApJ, 529, 786
 Nomoto, K., Sugimoto, D., Sparks, W. M., et al. 1982, Nature, 299, 803

Nagy, A., & Vinkó, J. 2016, *A&A*, 589, 53
 Nakaoka, T., Kawabata, K. S., Maeda, K., et al. 2018, *ApJ*, 859, 78
 Oke, J. B., Cohen, J. G., Carr, M., et al. 1995, *PASP*, 107, 375
 Olivares, F., Hamuy, M., Pignata, G., et al. 2010, *ApJ*, 715, 833
 Parker S., Kiyota, S., Morrell, N., et al., 2013, *Cent. Bur. Electron. Telegrams*, 3506, 1
 Pastorello, A., Sauer, D., Taubenberger, S., et al. 2006, *MNRAS*, 370, 1752
 Pastorello, A., Valenti, S., Zampieri, L., et al. 2009, *MNRAS*, 394, 2266
 Patat, F., Barbon, R., Cappellaro, E., & Turatto, M. 1993, *A&AS*, 98, 443
 Patat, F., Barbon, R., Cappellaro, E., & Turatto, M. 1994, *A&A*, 282, 731
 Planck Collaboration, et al. 2014, *A&A*, 571, 1
 Poon, H., Pun, J. C. S., Lam, T. Y., 2011, *arXiv.org:1109.0899*
 Popov D. V., 1993, *ApJ*, 414, 712
 Poznanski, D., Ganeshalingam, M., Silverman, J. M., & Filippenko, A. V. 2011, *MNRAS*, 415, L81
 Pritchard, T. A., Roming, P. W. A., Brown, P. J., et al. 2014, *ApJ*, 787, 157
 Richardson, D., Branch, D., Casebeer, D., et al. 2002, *AJ*, 123, 745
 Rodríguez, O., Pignata, G., Anderson, J., et al. 2020, *MNRAS*, 494, 5882
 Roming, P., Kennedy, T., Mason, K., et al. 2005, *Space Sci. Rev.*, 120, 95
 Rui, L. M., Wang, X. F., Mo, J., et al. 2019, *MNRAS*, 485, 1990
 Sahu, D. K., Anupama, G. C., Srividya, S., & Muneer, S. 2006, *MNRAS*, 372, 1315
 Sanders N. E., Soderberg, A. M., Gezari, S., et al. 2015, *ApJ*, 799, 208
 Schlafly, E. F., & Finkbeiner, D. P. 2011, *ApJ*, 737, 103
 Schlegel, E. M., 1990, *MNRAS*, 244, 269
 Schlegel, E. M., 1996, *AJ*, 111, 1660
 Schoniger, F., & Sofue, Y. 1994, *A&A*, 283, 21
 Shivvers, I., Groh, J. H., Mauerhan, J. C., et al. 2015, *ApJ*, 806, 213
 Smith, J., Tucker, D., Kent, S., et al. 2002, *AJ*, 123, 2121
 Spiro, S., Pastorello, A., Pumo, M. L., et al. 2014, *MNRAS*, 439, 2873
 Stritzinger, M. D., Anderson, J. P., Contreras, C., et al. 2018, *A&A*, 609, 134
 Stetson, P. 1987, *PASP*, 99, 191
 Suntzeff, N. B., & Bouchet, P., 1990, *AJ*, 99, 650
 Szalai, T., Vinkó, J., Könyves-Tóth, R., et al. 2019, *ApJ*, 876, 1
 Tartaglia, L., Pastorello, A., Sollerman, J., et al. 2020, *A&A*, 635, 39
 Tominaga, N., Blinnikov, S. I., & Nomoto, K. 2013, *ApJ*, 771, L12
 Tully, R. B., & Fisher, J. R. 1988, *Catalog of Nearby Galaxies* (Cambridge: Cambridge University Press)
 Turatto, M., Benetti, S., & Cappellaro, E. 2003, in *From Twilight to Highlight: The Physics of Supernovae*, ed. W. Hillebrandt & B. Leibundgut (Berlin: Springer-Verlag), 200
 Tutui, Y., & Sofue, Y. 1997, *A&A*, 326, 915
 Valenti, S., Sand, D., Stritzinger, M., et al. 2015, *MNRAS*, 2608, 2616
 Wang, C.-J., Bai, J.-M., Fan, Y.-F., et al. 2019, *RAA*, *arXiv:1905.05915*
 Wang, X., Li, W., Filippenko, A. V., et al. 2008, *ApJ*, 675, 626
 Woosley, S. E., Hartmann, D., & Pinto, P. A. 1989, *ApJ*, 346, 395
 Yaron, O., Perley, D. A., Gal-Yam, A., et al. 2017, *Nature Physics*, 13, 510
 Yuan, F., Jerkstrand, A., Valenti, S., et al. 2016, *MNRAS*, 465, 2003
 Zhang, J.-J., Yu, X.-G., & Wang, X.-F. 2018, *ATel*. #11379.

Zhang, J.-J., Wang, X.-F., Mazzali, P., et al. 2014, *ApJ*, 797, 5
 Zhang, T.-M., Wang, X.-F., Wu, C., et al. 2012, *AJ*, 144, 131

APPENDIX A: PHOTOMETRIC AND SPECTROSCOPIC DATA

This paper has been typeset from a $\text{\TeX}/\text{\LaTeX}$ file prepared by the author.

Table A1. Local photometric standard stars in the field of SN 2018zd^a

Star	<i>U</i> (mag)	<i>B</i> (mag)	<i>V</i> (mag)	<i>R</i> (mag)	<i>I</i> (mag)	<i>g</i> (mag)	<i>r</i> (mag)	<i>i</i> (mag)
1	14.88(0.01)	14.63(0.01)	13.79(0.01)	13.40(0.02)	13.02(0.02)	14.17(0.01)	13.56(0.01)	13.40(0.01)
2	15.47(0.01)	14.92(0.01)	13.98(0.01)	13.53(0.03)	13.12(0.01)	14.42(0.01)	13.68(0.01)	13.47(0.01)
3	16.35(0.02)	16.47(0.01)	15.93(0.02)	15.58(0.02)	15.26(0.02)	16.15(0.01)	15.78(0.01)	15.67(0.01)
4	16.49(0.01)	16.32(0.01)	15.54(0.03)	15.10(0.01)	14.69(0.01)	15.90(0.01)	15.31(0.01)	15.11(0.01)
5	17.54(0.04)	17.26(0.03)	16.41(0.03)	15.96(0.04)	15.53(0.02)	16.79(0.01)	16.18(0.01)	15.96(0.01)
6	15.48(0.02)	15.48(0.02)	14.80(0.02)	14.41(0.01)	14.04(0.01)	15.09(0.01)	14.61(0.01)	14.46(0.01)
7	17.08(0.01)	16.86(0.02)	16.06(0.02)	15.61(0.01)	15.19(0.02)	16.42(0.01)	15.82(0.01)	15.61(0.01)
8	17.48(0.02)	16.86(0.02)	15.92(0.01)	15.45(0.02)	15.03(0.02)	16.35(0.02)	15.61(0.01)	15.40(0.02)
9	17.94(0.01)	17.89(0.01)	17.08(0.01)	16.59(0.02)	16.13(0.02)	17.45(0.01)	16.83(0.01)	16.59(0.01)
10	14.56(0.01)	14.44(0.02)	13.72(0.01)	13.40(0.01)	13.08(0.01)	14.02(0.01)	13.56(0.01)	13.45(0.01)
11	17.26(0.03)	17.07(0.01)	16.27(0.01)	15.85(0.02)	15.46(0.03)	16.63(0.01)	16.04(0.01)	15.85(0.01)
12	16.85(0.01)	16.52(0.01)	15.67(0.01)	15.24(0.01)	14.83(0.03)	16.06(0.01)	15.42(0.01)	15.23(0.01)

^aSee Fig. 1 for the finder chart of these reference stars. *UBVRI* bands in Vega magnitude system, *gri* bands in AB magnitude system. Uncertainties (in parentheses) are 1σ .

Table A2. Ground-based photometry of SN 2018zd^a

Date (UT)	MJD	Epoch (d) ^b	<i>U</i> (mag)	<i>B</i> (mag)	<i>V</i> (mag)	<i>R</i> (mag)	<i>I</i> (mag)	<i>g</i> (mag)	<i>r</i> (mag)	<i>i</i> (mag)	Facility
Mar. 04 2018	58181.91	3.52	...	15.38(0.01)	15.26(0.01)	15.05(0.01)	14.91(0.01)	KOT
Mar. 05 2018	58182.76	4.37	...	14.93(0.01)	14.73(0.01)	14.79(0.01)	14.76(0.01)	14.87(0.01)	LJT
Mar. 07 2018	58184.70	6.31	13.30(0.02)	14.07(0.02)	13.91(0.01)	13.94(0.01)	13.96(0.01)	14.10(0.01)	LJT
Mar. 07 2018	58184.73	6.34	...	13.85(0.08)	13.96(0.05)	13.77(0.08)	13.73(0.05)	KOT
Mar. 08 2018	58185.48	7.09	...	13.93(0.01)	13.67(0.01)	13.59(0.01)	13.57(0.01)	TNT
Mar. 08 2018	58185.70	7.31	13.03(0.03)	13.82(0.02)	13.65(0.01)	13.68(0.01)	13.70(0.01)	13.85(0.02)	LJT
Mar. 08 2018	58185.75	7.36	...	13.70(0.05)	13.72(0.04)	13.52(0.10)	13.45(0.09)	KOT
Mar. 09 2018	58186.47	8.08	...	13.81(0.05)	13.51(0.10)	13.45(0.08)	13.43(0.09)	TNT
Mar. 09 2018	58186.70	8.31	12.98(0.03)	13.79(0.02)	13.55(0.01)	13.63(0.01)	13.62(0.01)	13.78(0.01)	LJT
Mar. 10 2018	58187.48	9.09	...	13.81(0.04)	13.49(0.04)	13.44(0.07)	13.40(0.04)	TNT
Mar. 10 2018	58187.79	9.40	...	13.75(0.03)	13.63(0.02)	13.46(0.03)	13.36(0.04)	KOT
Mar. 11 2018	58188.70	10.31	13.08(0.03)	13.86(0.01)	13.58(0.01)	13.69(0.01)	13.64(0.02)	13.74(0.01)	LJT
Mar. 12 2018	58189.47	11.08	...	13.93(0.04)	13.55(0.04)	13.46(0.09)	13.37(0.04)	TNT
Mar. 12 2018	58189.72	11.33	13.16(0.04)	13.94(0.03)	13.63(0.01)	13.75(0.01)	13.68(0.01)	13.79(0.01)	LJT
Mar. 12 2018	58189.74	11.35	...	13.76(0.07)	13.65(0.04)	13.46(0.07)	13.36(0.07)	KOT
Mar. 12 2018	58189.92	11.53	...	13.86(0.03)	13.71(0.02)	13.50(0.05)	13.36(0.07)	KOT
Mar. 13 2018	58190.64	12.25	13.21(0.02)	13.95(0.02)	13.64(0.01)	13.78(0.02)	13.68(0.01)	13.78(0.01)	LJT
Mar. 13 2018	58190.81	12.42	...	13.92(0.02)	13.76(0.01)	13.55(0.03)	13.39(0.04)	KOT
Mar. 14 2018	58191.77	13.38	...	14.00(0.02)	13.78(0.01)	13.56(0.03)	13.41(0.04)	KOT
Mar. 15 2018	58192.48	14.09	...	14.06(0.05)	13.65(0.04)	13.53(0.08)	13.46(0.05)	TNT
Mar. 18 2018	58195.47	17.08	...	14.19(0.04)	13.75(0.04)	13.57(0.07)	13.47(0.08)	TNT
Mar. 18 2018	58195.73	17.34	13.46(0.04)	14.18(0.01)	13.81(0.01)	13.95(0.01)	13.79(0.02)	13.85(0.01)	LJT
Mar. 19 2018	58196.48	18.09	...	14.21(0.05)	13.75(0.10)	13.59(0.07)	13.47(0.09)	TNT
Mar. 21 2018	58198.49	20.10	...	14.29(0.04)	13.83(0.05)	13.62(0.04)	13.48(0.06)	TNT
Mar. 21 2018	58198.56	20.17	13.55(0.03)	14.22(0.01)	13.83(0.01)	13.99(0.01)	13.81(0.01)	13.84(0.01)	LJT
Mar. 22 2018	58199.48	21.09	...	14.29(0.04)	13.83(0.03)	13.63(0.05)	13.48(0.04)	TNT
Mar. 22 2018	58199.78	21.39	...	14.25(0.02)	13.97(0.01)	13.68(0.03)	13.47(0.03)	KOT
Mar. 23 2018	58200.47	22.08	...	14.33(0.05)	13.85(0.06)	13.65(0.07)	13.50(0.05)	TNT
Mar. 23 2018	58200.61	22.22	13.66(0.03)	14.30(0.01)	13.89(0.01)	14.06(0.01)	13.83(0.02)	13.86(0.01)	LJT
Mar. 23 2018	58200.76	22.37	...	14.30(0.03)	13.99(0.02)	13.71(0.03)	13.51(0.03)	KOT
Mar. 23 2018	58200.87	22.48	...	14.24(0.05)	13.93(0.04)	13.66(0.06)	13.46(0.06)	KOT
Mar. 24 2018	58201.49	23.10	...	14.37(0.04)	13.87(0.05)	13.66(0.03)	13.49(0.04)	TNT
Mar. 24 2018	58201.84	23.45	...	14.29(0.04)	13.99(0.02)	13.70(0.04)	13.47(0.04)	KOT
Mar. 25 2018	58202.47	24.08	...	14.40(0.04)	13.89(0.07)	13.68(0.09)	13.49(0.07)	TNT
Mar. 25 2018	58202.67	24.28	13.75(0.03)	14.36(0.01)	13.93(0.01)	14.11(0.01)	13.85(0.01)	13.87(0.01)	LJT
Mar. 26 2018	58203.51	25.12	14.01(0.05)	13.76(0.09)	13.54(0.05)	TNT
Mar. 26 2018	58203.67	25.28	13.81(0.03)	14.38(0.02)	13.94(0.01)	14.14(0.02)	13.86(0.02)	13.86(0.02)	LJT
Mar. 29 2018	58206.67	28.28	13.95(0.02)	14.49(0.01)	14.00(0.01)	14.21(0.01)	13.91(0.01)	13.89(0.01)	LJT
Apr. 01 2018	58209.65	31.26	14.08(0.02)	14.55(0.02)	14.04(0.02)	14.27(0.02)	13.91(0.02)	13.87(0.02)	LJT
Apr. 02 2018	58210.67	32.28	14.14(0.03)	14.60(0.02)	14.05(0.02)	14.27(0.02)	13.92(0.02)	13.91(0.01)	LJT
Apr. 02 2018	58210.79	32.40	...	14.55(0.06)	14.11(0.04)	13.75(0.08)	13.48(0.07)	KOT
Apr. 02 2018	58210.82	32.43	...	14.61(0.02)	14.16(0.01)	13.80(0.02)	13.49(0.03)	KOT
Apr. 03 2018	58211.78	33.39	...	14.56(0.05)	14.13(0.03)	13.77(0.06)	13.48(0.06)	KOT
Apr. 08 2018	58216.48	38.09	...	14.80(0.05)	14.12(0.06)	13.81(0.04)	13.53(0.08)	TNT
Apr. 08 2018	58216.61	38.22	14.55(0.03)	14.78(0.02)	14.18(0.01)	14.45(0.02)	14.01(0.02)	13.89(0.03)	LJT
Apr. 08 2018	58216.80	38.41	...	14.77(0.03)	14.22(0.02)	13.84(0.05)	13.51(0.05)	KOT
Apr. 10 2018	58218.49	40.10	...	14.88(0.04)	14.15(0.04)	13.79(0.04)	13.54(0.10)	TNT
Apr. 11 2018	58219.49	41.10	...	14.91(0.06)	14.17(0.05)	13.83(0.08)	13.56(0.08)	TNT
Apr. 12 2018	58220.67	42.28	14.70(0.02)	14.88(0.02)	14.23(0.01)	14.53(0.01)	14.05(0.02)	13.99(0.01)	LJT

^aUncertainties (in parentheses) are 1σ .

^bThe epoch is relative to the explosion date, MJD = 58178.39.

Table A4. *Swift* UVOT photometry of SN 2018zd (Vega magnitude system)^a

Date (UT)	MJD	Epoch (d) ^b	<i>uvw</i> 2 (mag)	<i>uvm</i> 2 (mag)	<i>uvw</i> 1 (mag)	<i>u</i> (mag)	<i>b</i> (mag)	<i>v</i> (mag)
Mar. 04 2018	58181.29	2.90	16.00(0.04)	15.86(0.03)	15.53(0.04)	15.17(0.04)	16.17(0.04)	15.99(0.06)
Mar. 04 2018	58181.35	2.96	15.71(0.04)	15.68(0.06)	15.34(0.04)	15.01(0.04)	16.06(0.04)	15.82(0.06)
Mar. 05 2018	58182.35	3.96	14.10(0.02)	14.19(0.02)	14.03(0.02)	13.92(0.03)	15.04(0.03)	15.01(0.04)
Mar. 06 2018	58183.21	4.82	13.48(0.02)	13.49(0.06)	13.47(0.03)	13.43(0.03)	14.61(0.03)	14.56(0.04)
Mar. 07 2018	58184.28	5.89	13.07(0.11)	13.18(0.03)	13.25(0.11)	12.96(0.04)	14.21(0.04)	14.24(0.07)
Mar. 08 2018	58185.14	6.75	12.73(0.02)	12.88(0.03)	12.79(0.07)	12.69(0.03)	13.88(0.03)	13.84(0.04)
Mar. 10 2018	58187.23	8.84	12.86(0.02)	12.89(0.02)	12.77(0.07)	12.55(0.03)	13.71(0.02)	13.61(0.03)
Mar. 12 2018	58189.42	11.03	13.47(0.02)	13.28(0.02)	13.13(0.07)	12.78(0.03)	13.85(0.02)	13.68(0.03)
Mar. 14 2018	58191.74	13.35	13.85(0.02)	13.58(0.02)	13.28(0.07)	12.89(0.03)	13.92(0.03)	13.66(0.03)
Mar. 16 2018	58193.53	15.14	14.33(0.03)	13.99(0.03)	13.53(0.07)	13.02(0.03)	14.00(0.03)	13.75(0.03)
Mar. 18 2018	58195.85	17.46	14.56(0.02)	14.20(0.03)	13.76(0.07)	13.11(0.03)	14.05(0.02)	13.80(0.03)
Mar. 20 2018	58197.72	19.33	14.83(0.03)	14.49(0.03)	13.92(0.07)	13.22(0.03)	14.14(0.03)	13.86(0.03)
Mar. 30 2018	58207.34	28.95	16.01(0.04)	16.07(0.04)	15.03(0.07)	13.85(0.03)	14.41(0.03)	14.04(0.04)
Apr. 01 2018	58209.83	31.44	16.42(0.05)	16.55(0.05)	15.35(0.08)	13.98(0.03)	14.50(0.03)	14.08(0.04)
Apr. 05 2018	58213.41	35.02	17.01(0.05)	17.23(0.05)	15.77(0.08)	14.25(0.03)	14.63(0.03)	14.12(0.03)
Apr. 07 2018	58215.18	36.79	17.21(0.06)	17.71(0.07)	16.01(0.08)	14.38(0.03)	14.72(0.03)	14.21(0.04)
Apr. 19 2018	58227.13	48.74	18.16(0.15)	19.20(0.26)	17.16(0.14)	15.44(0.06)	14.96(0.04)	14.29(0.05)
Apr. 24 2018	58232.54	54.15	18.46(0.10)	19.18(0.14)	17.64(0.11)	15.64(0.04)	15.15(0.03)	14.38(0.03)
Apr. 30 2018	58238.74	60.35	18.80(0.11)	19.38(0.14)	17.82(0.11)	16.00(0.05)	15.34(0.03)	14.44(0.03)
May 06 2018	58244.72	66.33	18.87(0.12)	19.37(0.15)	18.14(0.12)	16.42(0.06)	15.50(0.03)	14.52(0.03)
May 12 2018	58250.25	71.86	18.79(0.11)	19.67(0.17)	18.31(0.13)	16.65(0.07)	15.61(0.03)	14.62(0.04)
May 18 2018	58256.55	78.16	19.29(0.17)	19.81(0.22)	18.64(0.16)	16.81(0.08)	15.73(0.03)	14.72(0.04)
May 24 2018	58262.92	84.53	19.24(0.19)	20.02(0.26)	18.64(0.17)	17.20(0.11)	15.93(0.04)	14.82(0.04)
Jun. 01 2018	58270.16	91.77	19.41(0.18)	...	18.23(0.18)	17.28(0.10)	16.16(0.03)	14.97(0.04)
Jun. 09 2018	58278.51	100.12	19.75(0.24)	...	18.92(0.21)	17.60(0.12)	16.23(0.04)	15.08(0.04)
Jun. 13 2018	58282.26	103.87	19.36(0.18)	...	19.36(0.18)	17.84(0.11)	16.44(0.04)	15.21(0.04)
Jun. 19 2018	58288.23	109.84	19.84(0.28)	...	18.92(0.35)	18.31(0.14)	16.74(0.04)	15.35(0.04)
Jun. 25 2018	58294.34	115.95	19.89(0.29)	...	19.24(0.30)	18.26(0.18)	16.78(0.12)	15.61(0.05)

^aUncertainties (in parentheses) are 1σ .^bThe epoch is relative to the explosion date, MJD = 58178.39.**Table A5.** Journal of spectroscopic observations of SN 2018zd

Date (UT)	MJD	Epoch (d) ^a	Range (Å)	Disp. (Å pix ⁻¹)	Exp (s)	airmass	Telescope+Inst.
Mar. 02, 2018	58179.61	1.22	3500–8900	2.85	2100	1.64	LJT+YFOSC
Mar. 04, 2018	58181.74	3.35	3500–8900	2.85	750	2.03	LJT+YFOSC
Mar. 05, 2018	58182.74	4.35	3500–8900	2.85	2100	2.00	LJT+YFOSC
Mar. 07, 2018	58184.69	6.30	3500–8900	2.85	1500	1.83	LJT+YFOSC
Mar. 09, 2018	58186.52	8.13	3960–8820	2.78	2400	1.30	XLT+BFOSC
Mar. 09, 2018	58186.71	8.32	3500–8900	2.85	1200	1.93	LJT+YFOSC
Mar. 10, 2018	58187.57	9.18	3500–8900	2.85	1500	1.62	LJT+YFOSC
Mar. 11, 2018	58188.68	10.29	3500–8900	2.85	1500	1.84	LJT+YFOSC
Mar. 13, 2018	58190.47	12.08	3980–8830	2.78	2100	1.27	XLT+BFOSC
Mar. 13, 2018	58190.62	12.23	3500–8900	2.85	1800	1.71	LJT+YFOSC
Mar. 15, 2018	58192.68	14.29	3500–8900	2.85	1500	1.87	LJT+YFOSC
Mar. 18, 2018	58195.74	17.35	3500–8900	2.85	1500	2.18	LJT+YFOSC
Mar. 20, 2018	58197.68	19.29	3500–8900	2.85	1500	1.94	LJT+YFOSC
Mar. 22, 2018	58199.53	21.14	3500–8900	2.85	1500	1.62	LJT+YFOSC
Mar. 24, 2018	58201.47	23.08	3960–8820	2.78	2400	1.29	XLT+BFOSC
Mar. 24, 2018	58201.71	23.32	3500–8900	2.85	1500	2.12	LJT+YFOSC
Mar. 29, 2018	58206.67	28.28	3500–8900	2.85	1800	2.04	LJT+YFOSC
Apr. 02, 2018	58210.69	32.30	3500–8900	2.85	1800	2.11	LJT+YFOSC
Apr. 13, 2018	58221.63	43.24	3500–8900	2.85	1300	2.01	LJT+YFOSC
Apr. 15, 2018	58223.53	45.14	3960–8820	2.78	2400	1.44	XLT+BFOSC
Apr. 23, 2018	58231.50	53.11	3450–8780	2.78	2700	1.42	XLT+BFOSC
Apr. 23, 2018	58231.68	53.29	3500–8900	2.85	1350	2.39	LJT+YFOSC
Apr. 27, 2018	58235.54	57.15	3960–8820	2.78	2400	1.53	XLT+BFOSC
Apr. 28, 2018	58236.51	58.12	3960–8820	2.78	2400	1.45	XLT+BFOSC
May 08, 2018	58246.50	68.11	4090–8800	2.78	2700	1.50	XLT+BFOSC
Aug. 30, 2018	58360.87	182.48	3500–8900	2.85	2100	1.96	LJT+YFOSC
Oct. 15, 2018	58406.73	228.34	3500–8900	2.85	2100	2.00	LJT+YFOSC
Oct. 30, 2018	58421.80	243.41	3980–8830	2.78	3000	1.27	XLT+BFOSC
Nov. 04, 2018	58426.18	247.79	5280–9300	2.29	1800	1.91	APO+DIS
Nov. 06, 2018	58428.71	250.32	3500–8900	2.85	2700	1.87	LJT+YFOSC
Nov. 18, 2018	58440.86	262.47	3860–8680	2.78	3600	1.33	XLT+BFOSC
Dec. 10, 2018	58462.40	284.01	5260–9400	2.30	1800	1.45	APO+DIS
Dec. 17, 2018	58469.79	291.40	3970–8830	2.78	3600	1.34	XLT+BFOSC
Nov. 01, 2019	58484.59	306.20	3850–8680	2.78	3600	1.28	XLT+BFOSC
Jan. 10, 2019	58493.61	315.22	3500–8900	2.85	3000	1.68	LJT+YFOSC
Feb. 02, 2019	58516.62	338.23	3500–8900	2.85	3600	1.68	LJT+YFOSC
Apr. 04, 2019	58577.27	398.88	3110–10300	0.91	940	2.06	Keck I+LRIS ^b

^aThe epoch is relative to the explosion date, MJD = 58178.39.^bBlue and red sides combined; parameters listed are the average values.

Table A6. Clear-band photometry of SN 2018zd (“Bright Supernovae”)^a

Date (UT)	MJD	Epoch (d) ^b	Mag	Observer
Mar. 01.54, 2018	58178.54	0.15	18.0	Koichi Itagaki
Mar. 02.49, 2018	58179.49	1.10	17.8	Koichi Itagaki
Mar. 03.49, 2018	58180.64	2.25	16.8	Koichi Itagaki
Mar. 03.64, 2018	58180.79	2.40	16.5	Koichi Itagaki
Mar. 03.79, 2018	58180.94	2.55	16.6	Koichi Itagaki
Mar. 04.53, 2018	58181.68	3.29	15.5	Yuji Tanaka
Mar. 06.54, 2018	58183.69	5.30	14.2	Yuji Tanaka
Mar. 06.71, 2018	58183.86	5.47	14.4	Koichi Itagaki
Mar. 14.45, 2018	58191.60	13.21	13.6	Yuji Tanaka

^awww.rochesterastronomy.org/sn2018/sn2018zd.html; uncertainties are ~ 0.1 mag, considering the translation between the clear band and the r band.

^bThe epoch is relative to the explosion date, MJD = 58178.39.